


RESEARCH ARTICLE | APRIL 10 2018

Shear-induced autorotation of freely rotatable cylinder in a channel flow at moderate Reynolds number


Yi Xia ; Jianzhong Lin; Xiaoke Ku; Tatleung Chan



Physics of Fluids 30, 043303 (2018)

<https://doi.org/10.1063/1.5021877>






Physics of Fluids

Special Topic:
Flow and Climate

Guest Editors: Khaled Ghannam and Mostafa Momen

Submit Today!



Shear-induced autorotation of freely rotatable cylinder in a channel flow at moderate Reynolds number

Yi Xia,¹ Jianzhong Lin,^{1,a)} Xiaoke Ku,¹ and Tatleung Chan²

¹State Key Laboratory of Fluid Power and Mechatronic Systems, Department of Mechanics, Zhejiang University, 310027 Hangzhou, China

²Department of Mechanical Engineering, The Hong Kong Polytechnic University, Hung Hom, Kowloon, Hong Kong

(Received 9 January 2018; accepted 24 March 2018; published online 10 April 2018)

Flow past a center-pinned freely rotatable cylinder asymmetrically confined in a two-dimensional channel is simulated with the lattice Boltzmann method for a range of Reynolds number $0.1 \leq Re \leq 200$, eccentricity ratio $0/8 \leq \varepsilon \leq 7/8$, and blockage ratio $0.1 \leq \beta \leq 0.5$. It is found that the inertia tends to facilitate the anomalous clockwise rotation of the cylinder. As the eccentricity ratio increases, the cylinder rotates faster in the counterclockwise direction and then slows down at a range of $Re < 10$. At a range of $Re > 40$, there exists an anomalous clockwise rotation for the cylinder at a low eccentricity ratio and the domain where the cylinder rotates anomalously becomes larger with the increase in the Reynolds number. In a channel with a higher blockage ratio, the rotation of the cylinder is more sensitive to the change of cylinder lateral position, and the separatrix at which the cylinder remains a state of rest moves upward generally. The cylinder is more likely to rotate counterclockwise and the rotating velocity is larger. At a lower blockage ratio, the anomalous clockwise rotation is more likely to occur, and the largest rotating velocity occurs when the blockage ratio is equal to 0.3. The mechanism of distinct rotational behavior of the cylinder is attributed to the transformation of distribution of shear stress which is resulted from the variation of pressure drop, the shift of maximum or minimum pressure zones along the upper and lower semi-cylinder surface, and the movement of stagnant point and separate point. Finally, the effects of the cylinder rotation on the flow structure and hydrodynamic force exerted on the cylinder surface are analyzed as well. *Published by AIP Publishing.* <https://doi.org/10.1063/1.5021877>

I. INTRODUCTION

Viscous flow past a cylinder is so ubiquitous both in nature and in the engineering field that it has been researched quite extensively and intensively. Among many branches of this problem, fluid-structure interaction is rather complicated to understand completely. The highly specialized subject of fluid structure interaction is vortex-induced vibrations (VIV), which has been comprehensively reviewed by Sarpkaya¹ and Williamson and Govardhan.² Another interesting subject is flow-induced rotation where autorotation, defined as a continuous rotation of a freely rotatable bluff in a parallel flow without external sources of energy, is the major issue.³ The present paper mainly addresses the anomalous autorotation of the center-pinned cylinder eccentrically situated in a two-dimensional channel. Interest in this flow arises not only from its application to the fields of industrial engineering such as the design of micropumps,^{4,5} but also from the point of view of understanding the particle rotational and translational behavior subjected to shear flow.^{6,7}

In contrast to a lot of research studies on the VIV, flow-induced rotation including autorotation has been relatively rarely studied. Lugt³ first addressed this issue and elucidated

clearly the definition and applications of autorotation. Lugt⁸ tried to understand the mechanism of autorotation through a set of numerical simulations of a parallel flow over an elliptic cylinder about a perpendicularly fixed axis and claimed that the synchronization of vortex shedding and rate of rotation are necessary conditions for autorotation. Asymmetrical pressure distribution on the cylinder induced by vortex shedding is a major motivation for the rotation of the unconfined cylinder. The square or rectangular cylinder was much preferred in research on autorotation before, despite that the circular cylinder plays a leading role in the flow past a bluff body. This is because pressure would not generate moments about the center of the circular cylinder for their identical intrinsic isotropy. Skews⁹ studied the effect of complex geography on the autorotation of the bluff body and found that the body of the triangular section rotates fastest and demonstrated that the phenomena of autorotation would occur only on the condition that the body has less than eight sides. Mittal *et al.*¹⁰ numerically studied the phenomenon of flutter (angular oscillations) and tumble (autorotation) of a two-dimensional pinned flat plate with rounded tips and indicated the strong dependence of the transition from flutter to tumble on the thickness ratio and the terminal velocity Reynolds number. The plate is more likely to tumble with increasing Reynolds number and decreasing thickness ratio. For a square cylinder free to rotate in a uniform flow, distinct rotation responses to the flow inertia have

^{a)}Author to whom correspondence should be addressed: mecjzlin@public.zju.edu.cn. Fax: 0086-571-87952882.

been characterized by Zaki *et al.*¹¹ and four characteristic rotational regimes have been named with respect to the Reynolds number, namely, stable position, oscillation, reversible rotation, and autorotation. Recently, Ryu and Iaccarino¹² enriched the rotation modes into six characteristic regimes through a parametric investigation. Apart from the “rest stable position” mode in a low Reynolds number regime and the “autorotation” mode in a high Reynolds number regime, four other modes have been mapped in moderate Reynolds regimes, namely, “small-amplitude oscillation,” “ $\pi/2$ -limit oscillation,” “random rotation,” and “ π -limit oscillation.” The associated moment generating mechanism has also been analyzed for the six distinct Reynolds number regimes in their work. Wang *et al.*¹³ investigated the effect of the distance between two freely rotatable triangular tandem cylinders on the dynamic behavior of the cylinders and vortical structure of the flow. Apart from an unusual vortex shedding pattern, they also found that the cylinders would show some irregular autorotation behaviors which are related to the terminal velocity Reynolds number, moment of inertia of the cylinders, and the cylinder spacing ratio.

The research studies mentioned above involve the non-circular cylinders. As for the rotation of the circular cylinder, it has received more and more attention for its benefit for flow control, drag reduction, vortex shedding suppression, and vibration suppression and results in its diverse application in the fields of aircraft, aeroballistics, biology, meteorology, and sports.^{14,15} Generally, the cylinder can be subjected to a forced-rotation or free-rotation, resulting in one-way or two-way coupling, respectively. The forced-rotation is an active flow control technique where an additional sustaining power is required and has been extensively addressed. A center-pinned, passive rotating cylinder is however with no need for extra energy and thus has been studied recently. Juarez *et al.*¹⁶ conducted the earliest detailed study on the flow over a freely rotatable cylinder. They carried out a direct simulation for a highly confined cylinder located at several eccentric positions based on high-order finite element methods, and the results show that the cylinder rotates in an opposite direction when its location moves from the vicinity of the wall to the channel centerline. The rotating direction depends strongly on the eccentricity and Reynolds number. They claimed that the presence of an eddy or a wake bubble attached behind an asymmetrically placed cylinder is contributed to the rotation in the opposite direction. The clockwise rotation of the cylinder placed far away from the wall in a high Reynolds number flow totally violates the claim that the angular velocity of particles is one half of the externally imposed shear rate by Einstein^{17,18} in a qualitative way. Similar anomalous rolling behavior of a totally free moving circular cylinder sedimenting in a two-dimensional channel was observed and analyzed much earlier. Goldman *et al.*¹⁹ first observed this anomalous rotation of spheres by studying the rotational motions of a sphere parallel to a plane wall bounding a semi-infinite, quiescent, viscous fluid. They found the sense of rotation of a sphere near a vertical wall and sedimenting in quiescent Newtonian fluid is the opposite of that in rolling at a wall without slipping. Liu *et al.*²⁰ and Singh and Joseph²¹ confirmed these anomalous rolling phenomena in both Newtonian and viscoelastic

liquids through both experiments and direct numerical simulation. Hu²² further addressed this issue numerically and performed a steady calculation for a uniform flow over a fixed cylinder confined in two sliding channel walls with a velocity of the approaching fluid to understand the mechanism for the rotation of a sedimenting cylinder in more detail and reported that the cylinder far away from the wall would experience a negative torque which drives it to rotate abnormally for a relatively large Reynolds number in a wide channel. For a three-dimensional cylinder, Seddon and Mullin²³ first studied the behavior of a heavy cylinder freely moving inside a rotating horizontal drum filled with a highly viscous fluid in the Stokes regime. The cylinder is observed to either co-rotate or counter-rotate depending on the rotating drum wall speed. They found a reverse rotation with increasing wall speed, which is anomalous. And by keeping increasing the wall speed further, the cylinder would back-spin slowly to rest and change the direction to co-rotate with the wall once more. Nevertheless, the co-rotation of the cylinder at high wall speed was not reported by Sun *et al.*²⁴ who extended this study experimentally in the Reynolds number ranging from 2500 to 25 000. As for the anomalous counter-rotation, they believed that it is due to the movements of the stagnation and separation points. Besides, they found a significant enhancement of the lift for the counter-rotation cylinder, which is believed to be caused by the vicinity of the wall. Apart from a single cylinder, a two-cylinder-flow system comes into researchers' sight recently. Tao and Bao²⁵ compared two side-by-side arranged rotatable cylinders with the stationary cylinder system via a characteristic-based split finite element method and found that the drag coefficient of the shear-driven rotating cylinders can be significantly reduced by 30.5% which is mainly contributed by a pressure drag for a gap ratio of 0.05 at $Re = 100$. They explained the drag-reduction mechanism in terms of a pressure-recovery effect introduced by shear-driven rotation and claimed that the cylinders' autorotation is attributed to the strong asymmetric distribution of the mean viscous shear stress on cylinders' surface with only little evidence attached. For the center-pinned confined cylinder, the region with abnormal rotation is far from the wall while it is near the wall for sedimenting particles or a freely moving cylinder. Lubrication force, which plays a critical role in the latter case, is not important in the present study. Nevertheless, the analysis of the shear stress and movements of the stagnation and separation points presented in these studies provide an improved insight into the physics analysis of the anomalous rotation of the center-pinned cylinder.

Based on the above description, we can see that there is a lack of research on the effects of the flow inertia and eccentricity on the shear-induced anomalous rotation of the center-pinned freely rotatable cylinder asymmetrically confined in a channel. Therefore, here we address such an issue that a viscous flow past a freely rotatable cylinder with its center axis pinned (center-pinned cylinder for short) in a two-dimensional channel. The purpose of this paper is to explore the dependence of center-pinned cylinder's rotation on the Reynolds number and eccentricity and elucidate the mechanism which the circular cylinders are induced to rotate, especially for the case of anomalous rotation (clockwise rotation in the present setup).

In addition, the effect of shear-induced rotation of the cylinder on the flow structure and hydrodynamic force exerted on the cylinder surface is discussed.

The remainder of this paper is organized as follows. Section II is dedicated to describe the problem studied here and corresponding mathematical formulation. In Sec. III, we furnish the reader with a brief introduction of the numerical method and a validation of algorithm is also conducted here. In Sec. IV, we present the numerical results along with some related discussions. Finally, the conclusions are drawn in Sec. V.

II. PROBLEM SETUP AND MATHEMATICAL FORMULATION

As shown in Fig. 1, the incompressible fluid flows past a center-pinned freely rotatable cylinder asymmetrically confined in a two-dimensional channel with height H and length $L = 30D$. The distances from the center of the cylinder to the inlet and outlet are $10D$ and $20D$, and such choices are believed to be able to minimize the impact of inlet and outlet boundary conditions on the interaction between the flow and the cylinder. The upper and lower walls are placed at $y = H/2$ and $y = -H/2$, respectively. The fluid flows from the left with a parabolic velocity profile $u_x = U_m \left[1 - 4\frac{y^2}{H^2}\right]$ to the right and $u_y = 0$. The eccentricity ratio $\varepsilon (\varepsilon = 2y/(H - D))$ is used to characterize the lateral position of the cylinder, and $\varepsilon = 0$ and 1 means that the cylinder is located at the centerline and at the position where the cylinder contacts the wall, respectively. The blockage ratio β is defined as $\beta = D/H$ as shown in Fig. 1. In the present study, the eccentricity ratio ε ranges from 0 to 7/8 and blockage ratio β ranges from 0.1 to 0.5, respectively. The density ratio of the cylinder to fluid is unity. The cylinder is only free to rotate around its center axis [Point O in Fig. 1(a)] with streamwise and lateral motion constrained. We only consider the case where the center-pinned cylinder is placed in the upper half of the channel for simplicity. So the

counterclockwise rotation [with respect to axis O, see Fig. 1(b)] of the pinned cylinder is the “normal” rotation, while the clockwise rotation [with respect to axis O, see Fig. 1(c)] is the anomalous rotation, as stated before.

Let Ω and Γ denote the domain occupied by fluid and the flowing boundary, respectively. The continuity and momentum equations are

$$\nabla \cdot \mathbf{u}^* = 0 \quad \text{in } \Omega, \quad (1)$$

$$\frac{\partial \mathbf{u}^*}{\partial t^*} + \mathbf{u}^* \cdot \nabla \mathbf{u}^* = \nabla \sigma^* \quad \text{in } \Omega, \quad (2)$$

where \mathbf{u}^* is the velocity, and the stress tensor $\sigma^* = -P^* + \tau^*$ [P^* is the pressure, the extra stress tensor $\tau^* = 2\mu S$, where μ is the viscosity, $S = (\mathbf{u}^* + \nabla \mathbf{u}^{*T})/2$].

Taking the cylinder diameter D and the centerline velocity at the channel inlet U_m as the characteristic length and characteristic velocity, respectively, and we have the following dimensionless equations:

$$\nabla \cdot \mathbf{u} = 0, \quad (3)$$

$$\frac{\partial \mathbf{u}}{\partial t} + \mathbf{u} \cdot \nabla \mathbf{u} = -\nabla P + \frac{1}{Re} \nabla^2 \tau, \quad (4)$$

where Reynolds number $Re = U_m D / \nu$ (ν is the kinematic viscosity of the fluid), $\mathbf{u} = \mathbf{u}^* / U_m$, $t = t^* U_m / D$, $P = 2P^* / \rho_f U_m^2$, and $\tau = 2\tau^* / \rho_f U_m^2$, and ρ_f is the fluid density.

Based on the theorem of angular momentum, the equation of the rotating cylinder is

$$J^* \frac{d\omega^*}{dt^*} = T^*, \quad (5)$$

where J^* is the moment of inertia about the center axis of the cylinder, ω^* is the rotating velocity of the cylinder, and T^* is the total torque exerted on cylinder by the fluid

$$T^* = \int_{\Gamma_p} (\sigma^* \cdot \mathbf{n}) \times (\mathbf{r}^* - \mathbf{r}_0^*) d\Gamma_p. \quad (6)$$

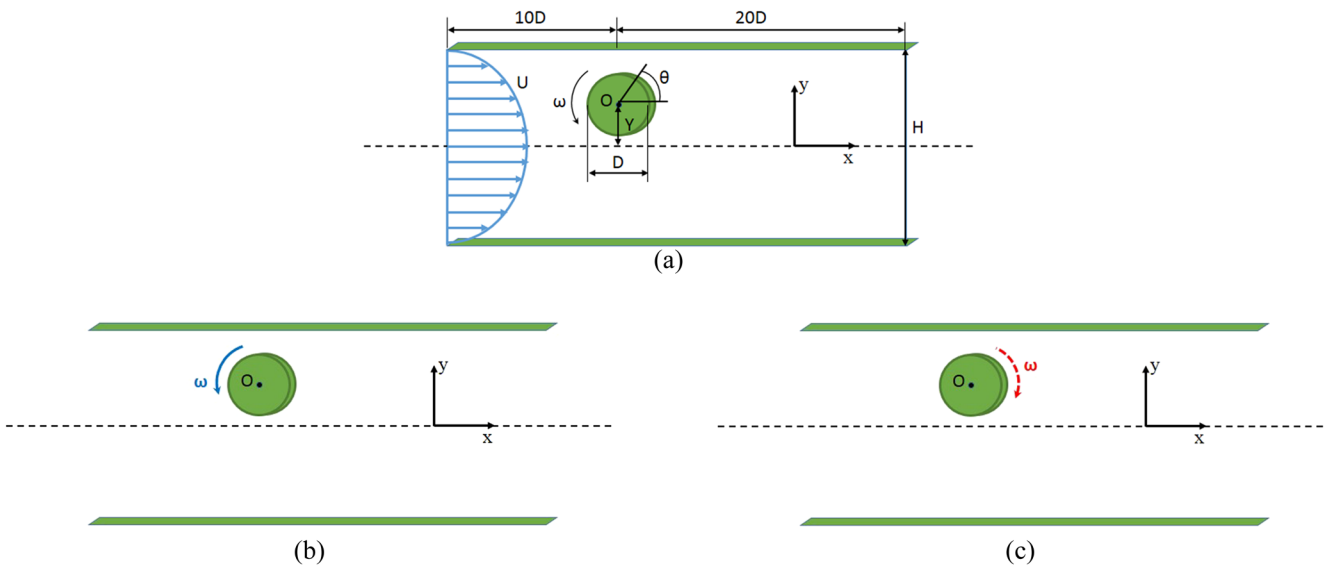


FIG. 1. (a) Schematic of a center-pinned cylinder eccentrically in a two-dimensional channel; (b) schematic of “normal” rotation; (c) schematic of “anomalous” rotation.

The drag force and lift force are defined as

$$F_L^* = \int_{\Gamma_p} (\sigma^* n) \cdot n_y d\Gamma_p, \quad F_D^* = \int_{\Gamma_p} (\sigma^* n) \cdot n_x d\Gamma_p. \quad (7)$$

Equation (5) can be non-dimensionalized

$$J \frac{d\omega}{dt} = C_T, \quad (8)$$

where J , ω , and C_T are

$$J = \frac{J^*}{\frac{1}{2}\rho_f \left(\frac{D}{2}\right)^2 \left(\frac{D}{2}\right)^2}, \quad \omega = \frac{\omega^* D}{2U_m}, \quad C_T = \frac{T^*}{\frac{1}{2}\rho_f U_m^2 D \cdot \frac{D}{2}}. \quad (9)$$

C_T is the torque coefficient. The drag, lift, and pressure coefficients are defined as

$$C_D = \frac{F_D^*}{\frac{1}{2}\rho_f U_m^2 D}, \quad C_L = \frac{F_L^*}{\frac{1}{2}\rho_f U_m^2 D}, \quad C_p = \frac{P - P_\infty}{\frac{1}{2}\rho_f U_m^2 D}. \quad (10)$$

III. NUMERICAL MODEL

There have been some numerical methods which were adopted to simulate the flow past cylinders. In these methods, the curved boundary should be handled with some specific technologies such as finite element method, finite volume method, immersed boundary method, dissipation particle dynamics, and smooth particle hydrodynamics. The lattice Boltzmann method based on the particle interaction has been proved to be an efficient direct numerical simulation method in recent decades.^{26,27}

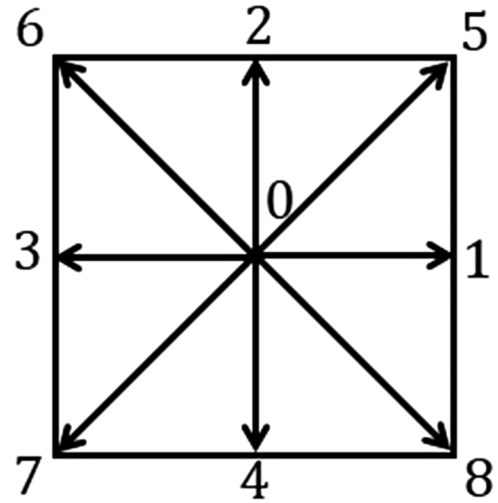


FIG. 2. D2Q9 model.

A. Lattice Boltzmann method

The lattice Boltzmann equation is stated below with a frequently used Bhatnagar-Gross-Krook collision model:

$$f_\alpha(\mathbf{x} + \mathbf{e}_\alpha \delta t, t + \delta t) - f_\alpha(\mathbf{x}, t) = -\frac{1}{\lambda} [f_\alpha(\mathbf{x}, t) - f_\alpha^{(eq)}(\mathbf{x}, t)], \quad (11)$$

where $f_\alpha(\mathbf{x}, t)$ is the distribution function at position \mathbf{x} and time t in the discrete velocity direction \mathbf{e}_α . λ is the dimensionless relaxation time, which is related to the fluid viscosity. It ranges from 0.56 to 0.8 in the present work. $f_\alpha^{(eq)}(\mathbf{x}, t)$ is the equilibrium distribution function (EDF). δx and δt are the lattice grid spacing and time increment, respectively, and set as $\delta x = \delta t = 1$. The two-dimensional nine-speed model (D2Q9),²⁸ as shown in Fig. 2, is used, and the particle velocity set reads as

$$\mathbf{e}_\alpha = \begin{cases} (0, 0) & \alpha = 0 \\ c \left(\cos[(\alpha - 1)] \frac{\pi}{2}, \sin[(\alpha - 1)] \frac{\pi}{2} \right) & \alpha = 1, 2, 3, 4, \\ \sqrt{2}c \left(\cos[(2\alpha - 1)] \frac{\pi}{4}, \sin[(2\alpha - 1)] \frac{\pi}{4} \right) & \alpha = 5, 6, 7, 8 \end{cases} \quad (12)$$

where c is the particle velocity $c = \delta x / \delta t$. The EDF is in the form

$$f_\alpha^{(eq)}(\mathbf{x}, t) = \rho w_\alpha \left[1 + \frac{\mathbf{e}_\alpha \cdot \mathbf{u}}{c_s^2} + \frac{(\mathbf{e}_\alpha \cdot \mathbf{u})^2}{2c_s^4} - \frac{\mathbf{u} \cdot \mathbf{u}}{2c_s^2} \right], \quad (13)$$

where $c_s = c/\sqrt{3}$ is the speed of sound in the lattice set and the weight coefficients are

$$w_\alpha = \begin{cases} \frac{4}{9} & \alpha = 0 \\ \frac{1}{9} & \alpha = 1, 3, 5, 7. \\ \frac{1}{36} & \alpha = 2, 4, 6, 8 \end{cases} \quad (14)$$

The local density and mass flux can be obtained by

$$\rho = \sum_{\alpha=0}^8 f_\alpha = \sum_{\alpha=0}^8 f_\alpha^{(eq)}, \quad (15)$$

$$\rho \mathbf{u} = \sum_{\alpha=0}^8 \mathbf{e}_\alpha f_\alpha = \sum_{\alpha=0}^8 \mathbf{e}_\alpha f_\alpha^{(eq)}.$$

The Navier-Stokes equation can be recovered by the Chapman-Enskog expansion with the kinematic viscosity $\nu = (2\lambda - 1)c^2\delta t/6$ and the pressure satisfies the equation of state as $P = \rho c_s^2$.

B. Boundary conditions and force evaluation

Boundary treatment at the solid-fluid interface is essential for guaranteeing the accuracy of calculation because the distribution functions streaming from solid nodes are missing. Despite the fact that the progress of the implementation of the boundary condition in terms of the distribution functions has been made over the years, the bounce-back scheme which was put forward in the early times is still the most popular method for efficiency and simplicity. The second-order unified interpolation bounce-back scheme²⁹ is adopted here as shown in Fig. 3 for the no-penetration and no-slip condition on the curved and moving boundary

$$f_{\alpha}(\mathbf{x}_f) = 1/(1 + \Delta) \left[\Delta f_{\alpha}(\mathbf{x}_{ff}) + (1 - \Delta) f_{\bar{\alpha}}(\mathbf{x}_f) + f_{\bar{\alpha}}(\mathbf{x}_b) + 2\omega_{\alpha}(\mathbf{e}_{\bar{\alpha}} \cdot \mathbf{u}_w)/c_s^2 \right], \quad (16)$$

where $f_{\bar{\alpha}}$ is the distribution function streaming in the inverse direction of f_{α} , $\mathbf{e}_{\bar{\alpha}} = -\mathbf{e}_{\alpha}$, $\Delta = \|\mathbf{x}_f - \mathbf{x}_w\|/\|\mathbf{x}_f - \mathbf{x}_b\|$ is the fraction of an intersected link in the fluid region.

To implement the channel flow, we adopt such a boundary condition as stated by Cheng and Luo.³⁰ For the inflow boundary, the parabolic velocity profile is set as stated in Sec. II. The distribution function is given as $f_{\alpha} = f_{\alpha}^{(eq)}(\rho_0, \mathbf{u})$, where $\rho_0 = 1$ is the mean density. At the outlet boundary, we assume that the flow is fully developed. The velocity at the outlet boundary lattice is extrapolated from the upstream lattice. A fixed pressure boundary is imposed here for the sake of numerical stability. And the flow is initialized through the equilibria of $f_{\alpha}^{(eq)}(\rho_0, \mathbf{u})$.

In order to study the fluid-solid interaction, it is quite important to accurately predict the force and torque exerted on the body by the fluid. There are generally three kinds of schemes for the calculation of the force, i.e., stress integration, momentum exchange, and volume fraction model. The scheme of momentum exchange is the most efficient one with considerable accuracy. In the present study, we use a novel Galilean-invariant momentum exchange method,³¹ as shown in the following equations, which are proved to be both

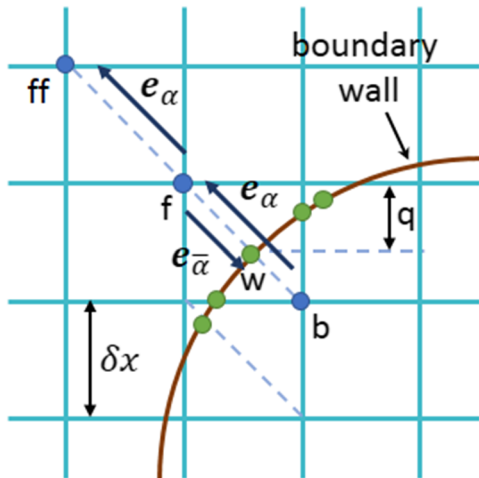


FIG. 3. The bounce-back scheme. \mathbf{x}_b : solid node; \mathbf{x}_w : wall node; \mathbf{x}_f : fluid node near \mathbf{x}_b ($\mathbf{x}_f = \mathbf{x}_b + \mathbf{e}_{\alpha}t$); \mathbf{x}_{ff} : fluid node ($\mathbf{x}_{ff} = \mathbf{x}_f + \mathbf{e}_{\alpha}t$).

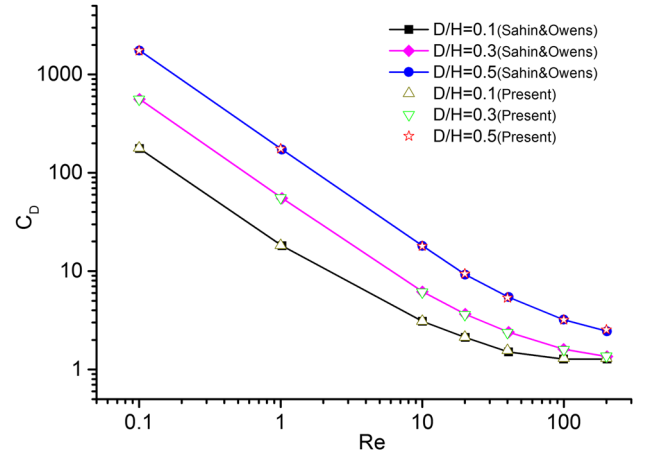


FIG. 4. Comparison of drag coefficient C_D versus Reynolds number Re for different blockage ratios β .

succinct and effective.^{32,33}

$$\mathbf{F} = \sum_{\alpha} \left\{ - \left[(\mathbf{e}_{\alpha} - \mathbf{u}_w) f_{\alpha}(\mathbf{x}_f) - (\mathbf{e}_{\bar{\alpha}} - \mathbf{u}_w) f_{\bar{\alpha}}(\mathbf{x}_f) \right] \right\}, \quad (17)$$

$$\mathbf{T} = \sum_{\alpha} \left\{ -(\mathbf{x}_w - \mathbf{x}_o) \times \left[(\mathbf{e}_{\alpha} - \mathbf{u}_w) f_{\alpha}(\mathbf{x}_f) - (\mathbf{e}_{\bar{\alpha}} - \mathbf{u}_w) f_{\bar{\alpha}}(\mathbf{x}_f) \right] \right\}. \quad (18)$$

C. Algorithm validation

In order to demonstrate the validity and precision of the model, we carry out several sets of trial calculations, in which the lattice density is $D/\delta x = 48$ in most cases (δx is lattice unit) considering the reliability and effectiveness of the calculation. First we perform the grid refinement to test the mesh independence, and then we conduct the computation of the flow past a static circular cylinder, which is a benchmark problem in computational fluid dynamics. For comparison purpose, we calculated the drag coefficient of a confined circular cylinder immersed in a channel flow for different Reynolds numbers and compared our results with the corresponding ones given by Sahin and Owens³⁴ as shown in Fig. 4. It is observed that the two results are very consistent for different confinement ratios. Furthermore, we calculated the drag coefficient and Strouhal number of a rotating circular cylinder in an unbounded flow to validate the effectiveness of the method in dealing with the problem of moving boundary. The comparison of the results is listed in Table I and it is seen that the present results are in good agreement with those available in the literature.^{35–40}

IV. RESULTS AND DISCUSSION

A. Instantaneous rotating velocity of cylinder

Figure 5 shows the rotating velocity ω of the center-pinned cylinder as a function of time T for different blockage ratios and eccentricity ratios. It can be seen that most rotating velocities converge to a certain value except the cases with considerable inertia as shown in Figs. 5(a), 5(c), and 5(d). At a high Reynolds number, there exists vortex shedding behind

TABLE I. Comparison of drag coefficient and Strouhal number ($\omega = 1$).

Source	C_D	Source	C_D	St
Re = 5		Re = 20		
Stojkovic <i>et al.</i> ³⁵	3.801	Badr <i>et al.</i> ³⁶	1.910	
Badr <i>et al.</i> ³⁶	3.810	Panda and Chhabra ³⁷	1.841	
Panda and Chhabra ³⁷	3.857	Paramane and Sharma ³⁸	1.837	
Present work	3.839	Present work	1.907	
Re = 40		Re = 100		
Panda and Chhabra ³⁷	1.323	Stojkovic <i>et al.</i> ³⁵	1.108	0.1658
Paramane and Sharma ³⁸	1.315	Kang <i>et al.</i> ³⁹	1.104	0.1655
Present work	1.321	Shaafia <i>et al.</i> ⁴⁰	1.178	0.1670
		Present work	1.159	0.1667

the cylinder, which would definitely lead to the change of the forces exerted on the cylinder surface and affect the evolution of the rotating velocity. The time that the rotating velocities converge to a certain value would be delayed with an increase in the Reynolds number. The flow is more stable when the cylinder is located closer to the walls (at high eccentricity ratio ε) because of the high confinement of no-slip boundary

condition and the fact that the fluid velocity between the cylinder and wall is very small.

B. Effect of Reynolds number on the mean rotating velocity

The mean rotating velocity $\bar{\omega}$ as a function of eccentricity ratio ε for different Reynolds numbers is shown in Fig. 6(a).

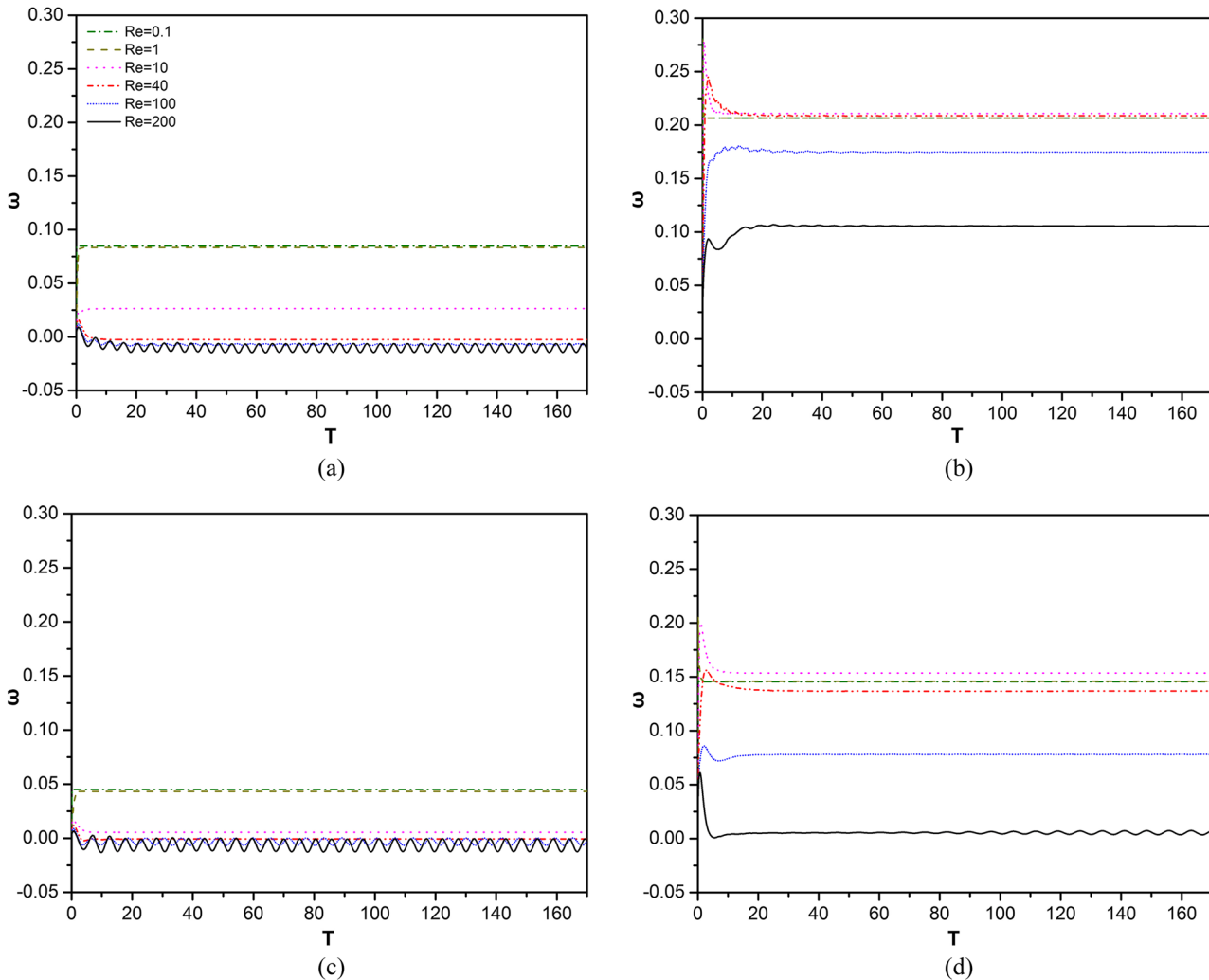


FIG. 5. Instantaneous rotating velocity ω of the cylinder. (a) $\beta = 0.3$, $\varepsilon = 1/8$; (b) $\beta = 0.3$, $\varepsilon = 7/8$; (c) $\beta = 0.2$, $\varepsilon = 1/8$; (d) $\beta = 0.2$, $\varepsilon = 7/8$.

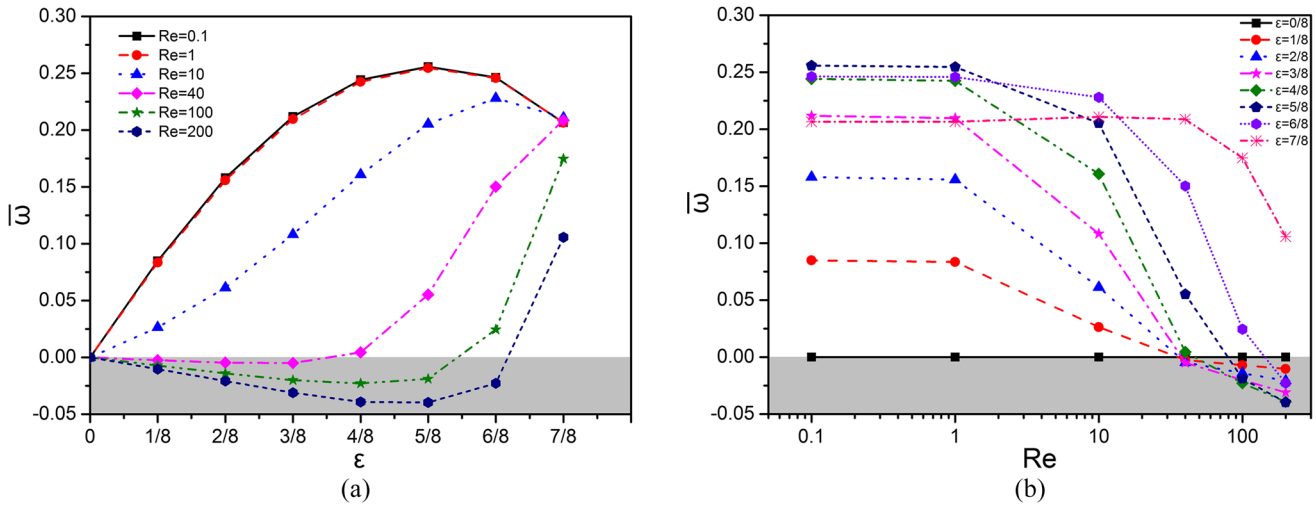


FIG. 6. Mean rotating velocity $\bar{\omega}$ as a function of eccentricity ratio ε and Reynolds number Re at blockage ratio $\beta = 0.3$.

Inertia plays a critical role in making the cylinder rotate in an abnormal way, which is analogous to the fact that a particle is driven to migrate laterally from the centerline in a channel. Actually, the rotating velocity of a freely moving particle would be altered in the case of large inertia.¹⁷ At small Reynolds numbers, as shown in the figure, the cylinder rotates counterclockwise and the direction of rotation is consistent with the general local fluid shear rate derived from the flow field in the absence of the cylinder, which is qualitatively in accordance with the law given by Einstein.¹⁷ The changes of mean rotating velocity $\bar{\omega}$ with eccentricity ratio ε are nearly the same for $Re = 0.1$ and 1, i.e., the inertia has scarcely any impact on the rotation of the cylinder in this range. A similar phenomenon was also reported by Hu.²² The mean rotating velocities get the same value for $Re = 0.1$, 1, 10, and 40 at $\varepsilon = 7/8$ although the process of their change is different, which indicated that the effect of the Reynolds number on the rotation of the cylinder is very small when the cylinder is located closer to the wall. When the Reynolds number increases and exceeds a certain value, the mean rotating velocities $\bar{\omega}$ decrease quickly with the increase in the Reynolds number Re as shown in Fig. 6(b), and finally changes from counterclockwise to clockwise at $Re = 40$ for $\varepsilon = 1/8-4/8$, $Re = 80$ for $\varepsilon = 5/8$, and $Re = 130$ for $\varepsilon = 6/8$, respectively. The inertia tends to facilitate the clockwise rotation of the cylinder. This abnormal phenomenon violates the law given by Einstein.¹⁸

C. Effect of eccentricity ratio on the mean rotating velocity

The eccentricity ratio, which characterizes the distance from the cylinder to the wall, has a large impact on the rotation of the cylinder. The mean rotating velocity $\bar{\omega}$ as a function of Reynolds number Re for different eccentricity ratios ε is shown in Fig. 6(b). The cylinder would hardly rotate if it is placed at the centerline ($\varepsilon = 0$) because there are scarcely any net moments acting on the cylinder due to the symmetry of the flow field and cylinder geometry. Even if the Reynolds numbers are very large, the cylinder only rotates back and

forth with the rotating velocity oscillating near zero. In the vicinity of the wall ($\varepsilon = 7/8$), the cylinder always rotates in the direction which is consistent with the general local fluid shear rate derived from the flow field. This is attributable to the confinement of the wall and the weak fluid inertia in this region. At $Re < 1$, the cylinder rotates counterclockwise with a constant mean rotating velocity, which increases with a decrease in the distance between the cylinder and the wall, except the case in the vicinity of the wall ($\varepsilon = 7/8$ and $6/8$). At $Re = 10$, the varying tendency of mean rotating velocity with respect to the eccentricity ratio is similar to that at $Re < 1$. Nevertheless, at $Re > 40$, the cylinder begins to rotate clockwise in the region near the channel centerline. The mean rotating velocities decrease at first and then increase after reaching a trough, as the eccentricity ratio increases from $\varepsilon = 0$ to $\varepsilon = 7/8$.

D. Effect of blockage ratio on the mean rotating velocity

Figure 7 shows the comprehensive influence of wall constraint on the mean rotating velocity $\bar{\omega}$ of the cylinder. In a higher blockage ratio channel, the rotation of the cylinder is more sensitive to the position of the cylinder because the velocity profile is steeper and the variation of local shear rate is larger. In a lower blockage ratio channel, the rotating directions of the cylinder are invariably counterclockwise at $Re = 40$ as shown in Fig. 7(a) or invariably clockwise at $Re = 100$ as shown in Fig. 7(b) even if the cylinder is placed closer to the wall. The counterclockwise rotating velocity $\bar{\omega}$ increases with an increase in the blockage ratio β . All maximum counterclockwise rotating velocity occurs in the vicinity of the wall except the case for $\beta = 0.5$ at $Re = 40$ as shown in Fig. 7(a). It is more complex for the abnormal rotation of the cylinder. The maximum clockwise rotating velocity does not occur in the case with the minimum blockage ratio even though the cylinder is most likely to rotate clockwise in this case, but it occurs in the case with an intermediate blockage ratio of $\beta = 0.3$ at $Re = 100$ as shown in Fig. 7(b). It shows that the critical point at which the abnormal rotation of the

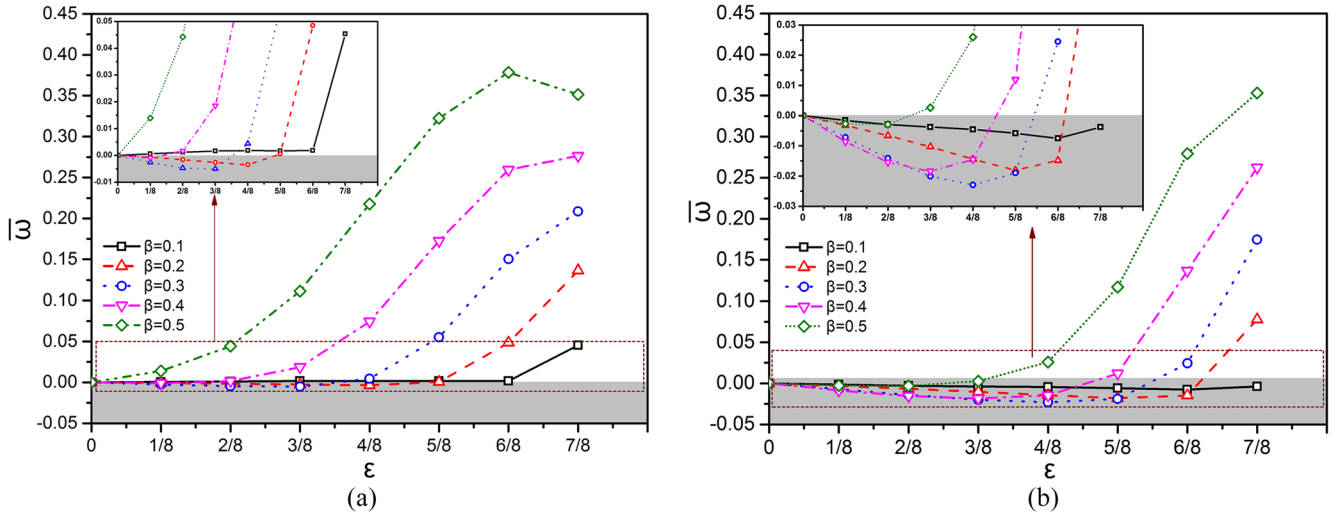


FIG. 7. Mean rotating velocity $\bar{\omega}$ as a function of eccentricity ratio ε for different blockage ratios β . (a) $Re = 40$ and (b) $Re = 100$.

cylinder occurs (from counterclockwise to clockwise) is at an intermediate blockage ratio and intermediate eccentricity ratio.

E. Phase space diagram for the rotational behavior of the cylinder

In order to further understand the dependence of cylinder rotation on the inertia, eccentricity, and wall constraint, a phase space diagram for the rotational behavior of the cylinder is drawn in Fig. 8. There exists another separatrix at which the torque-free center-pinned cylinder remains static, apart from the centerline. As a result, the half channel can be divided into two distinct regions. In the region between the separatrix and the wall, the cylinder rotates counterclockwise, which is analogous to the case with a low Reynolds number. For the case with a high blockage ratio, viscosity plays a dominant role in this region. The cylinder rotates clockwise in the region between the separatrix and the centerline, which is an abnormal rotation. When the position of the cylinder is moved from the centerline to the separatrix, the cylinder rotates faster in a clockwise direction and then slows down after reaching a

maximum. With increasing the Reynolds number, the maximum clockwise rotating velocity becomes larger and the position where the rotating velocity reaches its maximum shifts toward the wall.

The effects of Reynolds number, eccentricity ratio, and blockage ratio can be delineated qualitatively from the critical separatrix line. Generally, the critical Reynolds number is low when the cylinder is located near the channel centerline and increases accordingly with an increase in the eccentricity ratio. It should be noted that although the rotating velocity of the cylinder would reach a trough at an intermediate eccentricity ratio, there does not exist a trough for critical Reynolds number in the range of eccentricity ratio ($1/8 \leq \varepsilon \leq 7/8$) for both blockage ratios $\beta = 0.2$ and $\beta = 0.3$. The critical Reynolds number remains unchanged with the eccentricity ratio ε varying from $1/8$ to $4/8$ at $\beta = 0.2$ and then increases gradually as the eccentricity ratio ε further increases. For the cases with a high blockage ratio, the critical Reynolds number is more sensitive to the variation of eccentricity ratio due to the fact that the velocity profile in this case is much steeper. And the separatrix generally moves upward when the blockage effect becomes more severe.

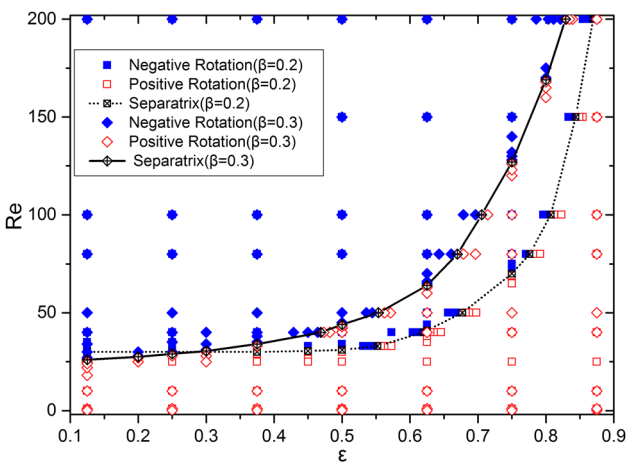


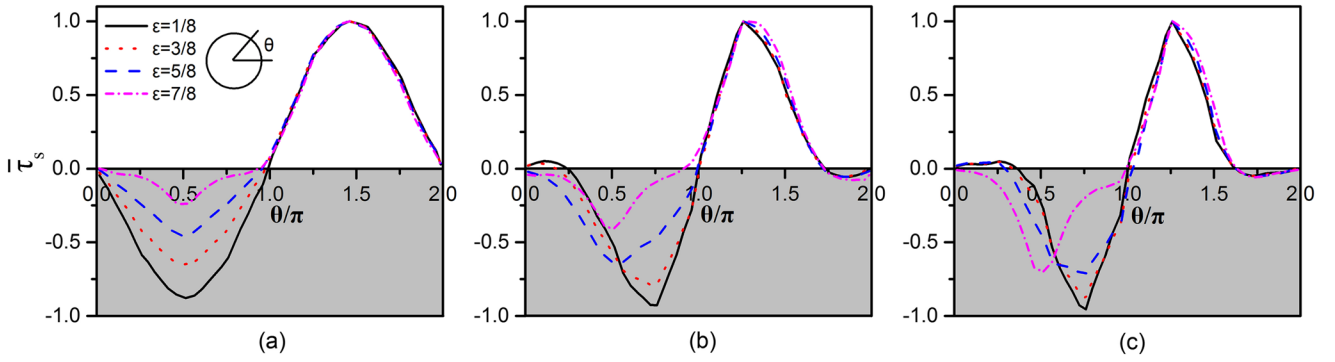
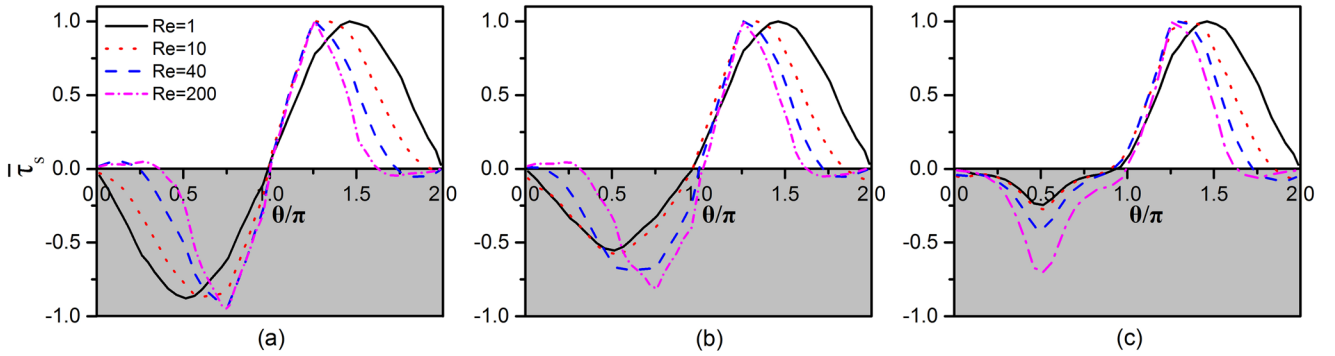
FIG. 8. Phase diagram for the rotational behavior of the cylinder.

F. Mechanism of rotational behavior of cylinder

In order to elucidate the mechanism of the rotation of the center-pinned cylinder, it is not suitable to take a rotating cylinder as a research object because the torque exerted on the cylinder by the fluid will change for a rotating cylinder. Therefore, we perform a series of simulations with keeping the cylinder at static and setting other parameters to be the same as those for the rotating cylinder.

1. Distributions of shear stress

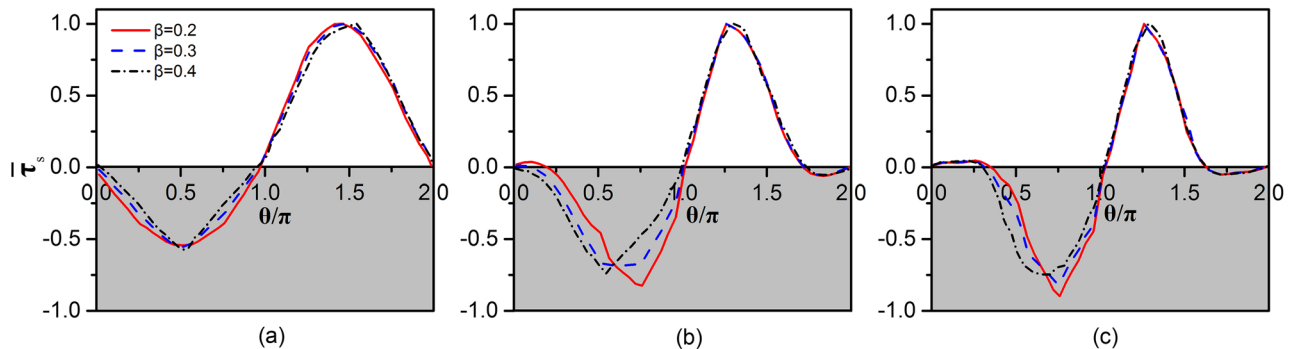
The distributions of shear stress $\bar{\tau}_s$, which play a crucial role in driving the cylinder to rotate, are shown in Figs. 9–11 through a physical decomposition method.⁴¹ The stress is averaged over time since it would oscillate with time T especially at a high Reynolds number. It is worth mentioning that the competition between positive shear stress and negative shear

FIG. 9. Normalized mean shear stress $\bar{\tau}_s$ exerted on the static cylinder at $\beta = 0.3$. (a) $Re = 1$; (b) $Re = 40$; (c) $Re = 200$.FIG. 10. Normalized mean shear stress $\bar{\tau}_s$ exerted on the static cylinder at $\beta = 0.3$. (a) $\epsilon = 1/8$; (b) $\epsilon = 4/8$; (c) $\epsilon = 7/8$.

stress determines the rotating behavior of the cylinder. Note that the stress $\bar{\tau}_s$ as shown in Figs. 9–11 is normalized by its maximum positive shear stress since only the relative values are meaningful for interpreting the mechanism of rotational behavior of the cylinder. From the figures, we can see that the half surfaces of the cylinder near the centerline and the wall are mainly subjected to the positive and negative shear stress, respectively. The maximum values of the positive and negative shear stress occur in the position with the azimuthal angle $\theta \approx \pi/2$ and $3\pi/2$, respectively, which is more obvious at a low Reynolds number as shown in Fig. 10. Normally, the positive shear stress drives the cylinder to rotate counterclockwise, while the rotational behavior is dependent on the Reynolds number Re , eccentricity ratio ϵ , and blockage ratio β .

In Fig. 9, the positive shear stresses $\bar{\tau}_s$ exerted on the half surfaces of the cylinder near the centerline (i.e., $\pi < \theta < 2\pi$) are nearly the same for different eccentricity ratios at a specific Reynolds number, while absolute values of negative shear stresses $\bar{\tau}_s$ on the half surfaces of the cylinder near the wall (i.e., $0 < \theta < \pi$) decrease with an increase in the eccentricity ratio. In the vicinity of the centerline ($\epsilon = 1/8$), the shear stress has an anti-symmetry distribution, while in the vicinity of the wall ($\epsilon = 7/8$), the positive shear stress is much larger than the negative shear stress, which makes the cylinder rotate counterclockwise.

The effect of the Reynolds number Re on the shear stress $\bar{\tau}_s$ is more clearly displayed in Fig. 10. The difference in the values between the positive and negative shear stress decreases with the increase of the Reynolds number, which indicates that

FIG. 11. Normalized mean shear stress $\bar{\tau}_s$ exerted on the static cylinder at $\epsilon = 4/8$. (a) $Re = 1$; (b) $Re = 40$; (c) $Re = 200$.

the inertia tends to reduce the difference of shear stress exerted on the upper and lower semi-cylinder surface. Therefore, the rotating velocity $\bar{\omega}$ of the cylinder decreases as the Reynolds number Re increases as shown in Fig. 6(b). In the figure, the positive shear stress is larger than the negative shear stress even at a high Reynolds number. However, it is well worth noticing that, at a high Reynolds number, the surface area subjected to the negative shear stress is larger than that subjected to the positive shear stress because the shift of the recirculation zone breaks the symmetry of the flow. Both the front and rear stagnant points shift azimuthally to the channel centerline, resulting in the enlargement and reduction of the surface area subjected to the negative and positive shear stress, respectively. So the torque exerted on the cylinder produced by the negative shear stress would exceed that by the positive shear stress. The competition between the above two factors makes the occurrence of anomalous rotation of the cylinder at a high Reynolds number.

The blockage ratio β has a smaller effect on the shear stress $\bar{\tau}_s$ especially at a low Reynolds number as shown in Fig. 11. At $Re = 1$, the shear stresses $\bar{\tau}_s$ are nearly the same for different blockage ratios β . At $Re = 200$, the negative shear stress slightly decreases with an increase in the blockage ratio, which makes the cylinder rotate counterclockwise faster.

2. Distributions of maximum shear stress

The dependence of maximum positive shear stress $|\bar{\tau}_{s+}|_{MAX}$ and negative shear stress $|\bar{\tau}_{s-}|_{MAX}$ on the Reynolds number Re , eccentricity ratio ε , and blockage ratio β is shown in Fig. 12. $\Delta|\bar{\tau}_{s+}|_{MAX}(\%)$ and $\Delta|\bar{\tau}_{s-}|_{MAX}(\%)$ are the relative value of the maximum positive and negative shear stress to that at the centerline, respectively. The increase in $|\bar{\tau}_{s+}|_{MAX}$ and $|\bar{\tau}_{s-}|_{MAX}$ would facilitate the cylinder to rotate counterclockwise and clockwise, respectively.

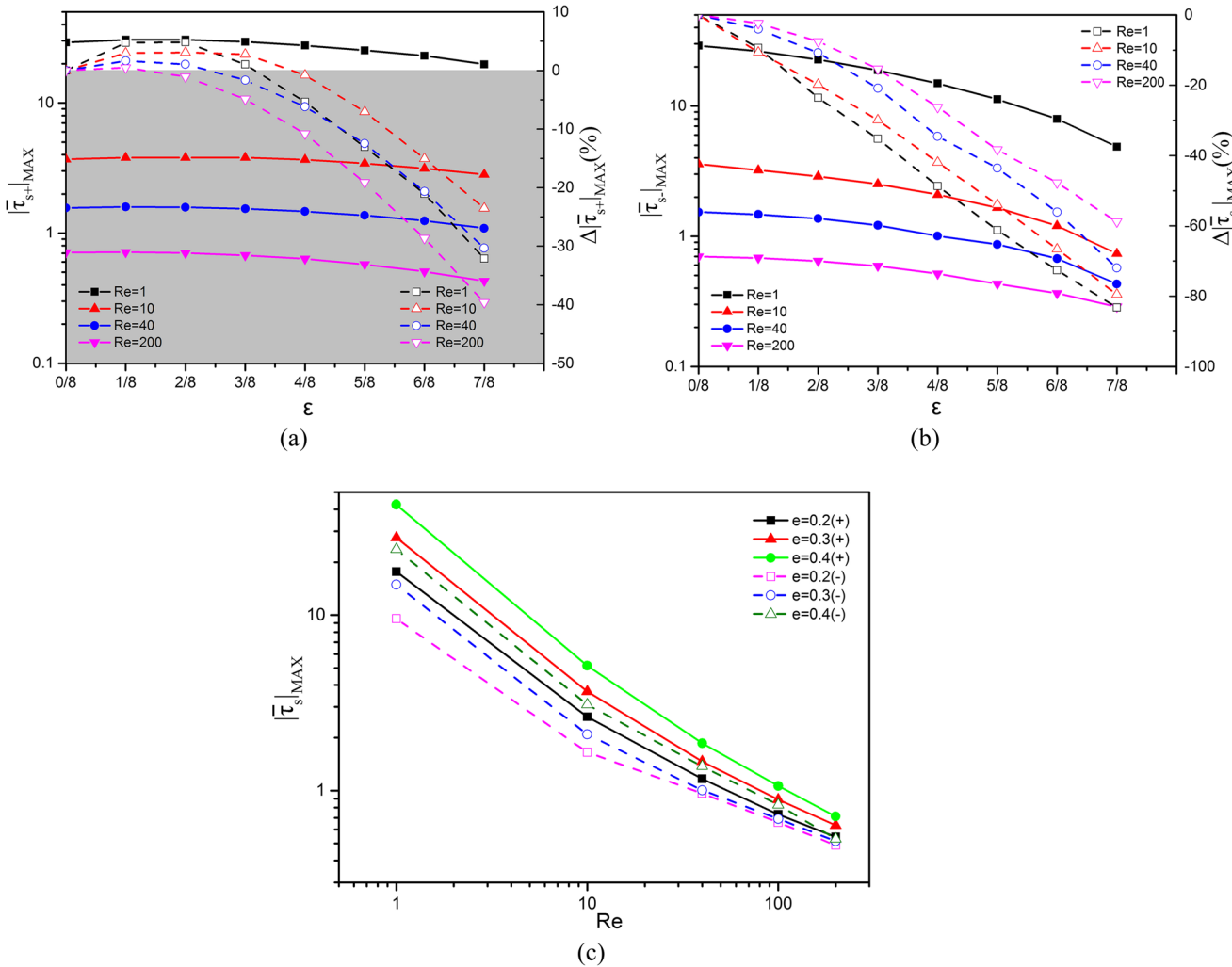


FIG. 12. Maximum values of shear stress on the static cylinder. (a) Maximum positive shear stress ($\beta = 0.3$). $|\bar{\tau}_{s+}|_{MAX}$: maximum positive shear stress; $\Delta|\bar{\tau}_{s+}|_{MAX}(\%)$: relative value of maximum positive shear stress to that at the centerline; $|\bar{\tau}_{s+}|_{MAX}$: black filled squares, red filled triangles, blue filled circles, and pink filled down-pointing triangles; $\Delta|\bar{\tau}_{s+}|_{MAX}(\%)$: black squares, red triangles, blue circles, and pink down-pointing triangles. (b) Maximum negative shear stress ($\beta = 0.3$). $|\bar{\tau}_{s-}|_{MAX}$: maximum negative shear stress; $\Delta|\bar{\tau}_{s-}|_{MAX}(\%)$: relative value of maximum negative shear stress to that at the centerline; $|\bar{\tau}_{s-}|_{MAX}$: black filled squares, red filled triangles, blue filled circles, and pink filled down-pointing triangles; $\Delta|\bar{\tau}_{s-}|_{MAX}(\%)$: black squares, red triangles, blue circles, and pink down-pointing triangles. (c) $\varepsilon = 4/8$. [(+): Positive shear stress; (-): Negative shear stress].

As shown in Fig. 12(a), $|\bar{\tau}_{s+}|_{\text{MAX}}$ decreases slightly with an increase in the eccentricity ratio ε for different Reynolds numbers Re , but reduces significantly with an increase in the Reynolds number Re for different eccentricity ratios ε . The variation of $\Delta|\bar{\tau}_{s+}|_{\text{MAX}}(\%)$ is more complicated. At $0 < \varepsilon < 2/8$, $\Delta|\bar{\tau}_{s+}|_{\text{MAX}}(\%)$ declines with increasing the Reynolds number, while it first slightly increases and then remains unchanged or slightly decreased with an increase in the eccentricity ratio. At $\varepsilon > 2/8$, $\Delta|\bar{\tau}_{s+}|_{\text{MAX}}(\%)$ decreases with increasing the eccentricity ratio, but it does not change monotonously with the Reynolds number, which indicates that $\Delta|\bar{\tau}_{s+}|_{\text{MAX}}(\%)$ is dependent on the comprehensive effect of the wall constraint and fluid inertia.

As shown in Fig. 12(b), the decrease in $|\bar{\tau}_{s-}|_{\text{MAX}}$ with an increase in the eccentricity ratio is more obvious than that of $|\bar{\tau}_{s+}|_{\text{MAX}}$ for different Reynolds numbers. The main difference between $\Delta|\bar{\tau}_{s-}|_{\text{MAX}}(\%)$ and $\Delta|\bar{\tau}_{s+}|_{\text{MAX}}(\%)$ is that the former decreases monotonously with increasing the eccentricity ratio and decreasing the Reynolds number.

As shown in Fig. 12(c), the maximum positive shear stress $|\bar{\tau}_{s+}|_{\text{MAX}}$ is always larger than the maximum negative shear stress $|\bar{\tau}_{s-}|_{\text{MAX}}$ for a definite blockage ratio β . As a result, the cylinder rotates counterclockwise. Both maximum positive and negative shear stresses decrease with reducing the blockage ratio and increasing the Reynolds number, which is consistent with the well-known rule of the relationship between drag, pressure coefficient, and Reynolds number.

3. Distributions of mean pressure coefficient

The rotation of the center-pinned cylinder is mainly attributed to the shear stress exerted on the cylinder surface, while the distribution of the shear stress distribution is highly related to the pressure field. To make a further understanding of the rotational behavior, the pressure distributions and contours on the cylinder surface are shown in Figs. 13–15 in polar coordinate form and Fig. 16, respectively.

When the cylinder is eccentrically situated at a low Reynolds number, the minimum pressure zones shift clockwise and are not directly behind the cylinder as shown in Figs. 13(a) and 16(a), which makes the positive shear stress play a dominant role in driving the cylinder to rotate

counterclockwise. The pressure drop decreases sharply as the Reynolds number increases as shown in Figs. 13 and 16, which results in the decrease in the shear stress.

As shown in Fig. 13, as the Reynolds number increases, the single minimum pressure zone behind the cylinder breaks into two pieces. In addition, both minimum pressure zones together with the maximum pressure zone shift azimuthally along the cylinder surface. The maximum pressure zone shifts counterclockwise with a small angle. The two minimum pressure zones shift windward along both upper and lower semi-cylinders, and the moving of the minimum pressure zone on the upper semi-cylinder lags slightly behind the one on the lower semi-cylinder. Such an asymmetric distribution of the minimum pressure zone, accompanied by the leeward moving of the maximum pressure zone, produces a difference in the surface areas subjected to the negative and positive shear stress. As the Reynolds number increases further, the two minimum pressure zones are more symmetrical and their values are close to be the same level. Therefore, the difference in the values between the positive and negative shear stress decreases as the Reynolds number increases.

The distribution of mean pressure coefficient \bar{C}_p on the cylinder surface at different eccentricity ratios ε is shown in Fig. 14. The maximum pressure decreases with the increase in the eccentricity ratio. Comparing Fig. 16(c) with Fig. 16(d), as the eccentricity ratio ε increases, the minimum pressure zone on the upper semi-cylinder becomes smaller and finally disappears, while that on the lower semi-cylinder becomes larger. Consequently, the pressure drop along the lower semi-cylinder is much larger than that along the upper semi-cylinder at higher eccentricity ratio β , which makes the positive shear stress play a dominant role in this region. Meanwhile, the maximum pressure zone shifts counterclockwise and the minimum pressure zone on the upper semi-cylinder shifts leeward, leading to a variation of cylinder surface areas subjected to the positive and negative shear stress. The rotational behavior of the cylinder is dependent on the competition of both factors mentioned above.

Figures 15, 16(e), and 16(f) show the distribution of mean pressure coefficient at different blockage ratios β . The pressure difference becomes larger with the increase of the blockage ratio. There is no apparent shift of maximum and minimum pressure zones. In a conclusion, the rotational behavior of the

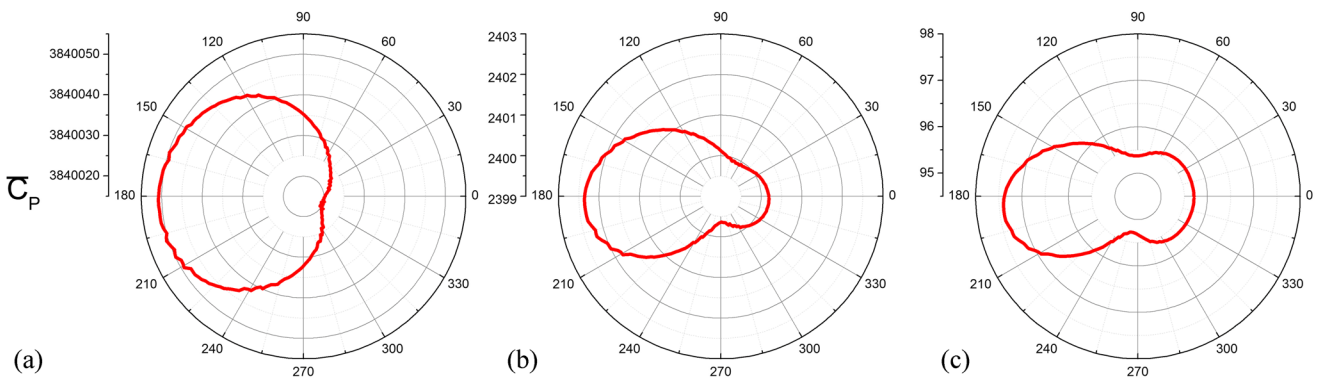


FIG. 13. Distribution of mean pressure coefficient \bar{C}_p on the cylinder surface at $\varepsilon = 4/8$ and $\beta = 0.3$. (a) $Re = 1$; (b) $Re = 40$; (c) $Re = 200$.

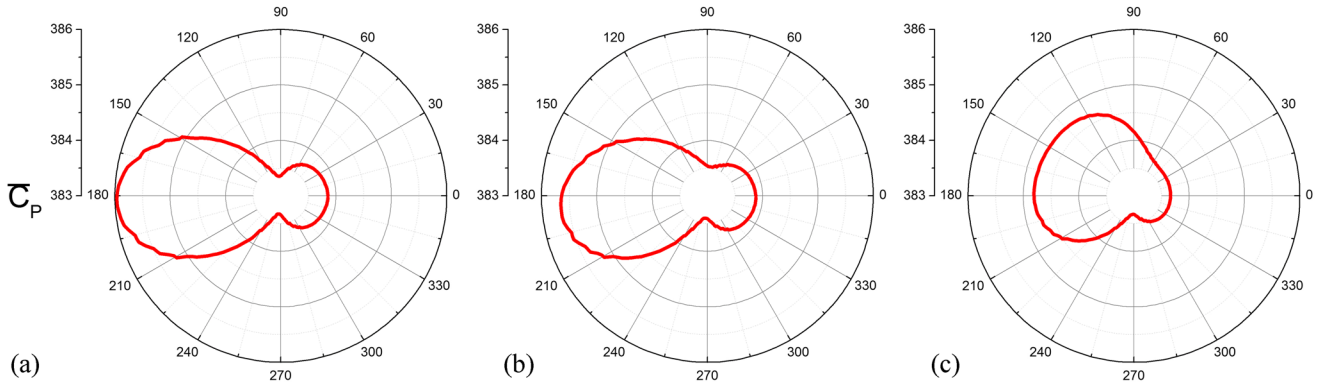


FIG. 14. Distribution of mean pressure coefficient \bar{C}_p on the cylinder surface at $Re = 100$ and $\beta = 0.3$. (a) $\varepsilon = 1/8$; (b) $\varepsilon = 4/8$; (c) $\varepsilon = 7/8$.

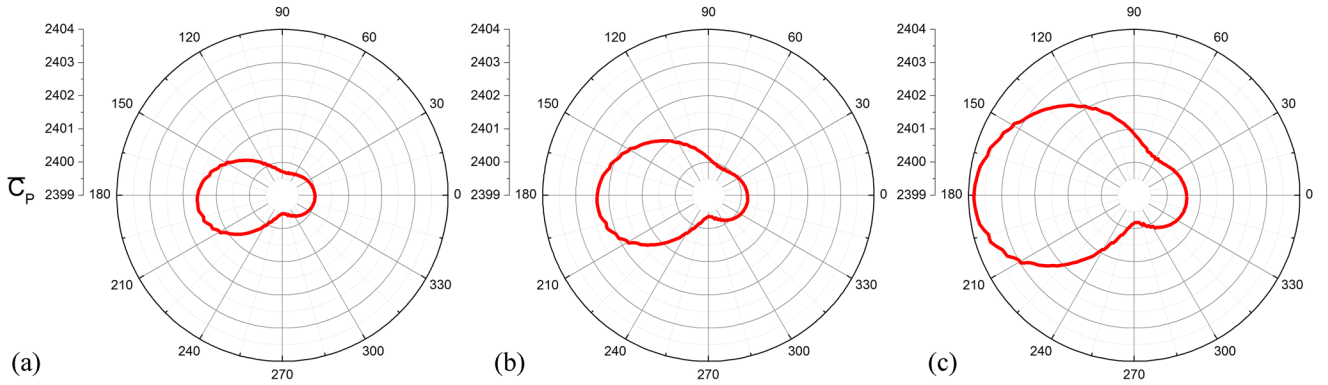


FIG. 15. Distribution of mean pressure coefficient \bar{C}_p on the cylinder surface at $Re = 40$ and $\varepsilon = 4/8$. (a) $\beta = 0.2$; (b) $\beta = 0.3$; (c) $\beta = 0.4$.

cylinder is dependent on the distribution of shear stress exerted on the cylinder, while shear stress is affected by the factors including the pressure difference on the cylinder surface, the shift of maximum and minimum pressure zones, and the shift of stagnant points and separate points. Certainly, these factors are highly related to the Reynolds number Re , eccentricity ratio ε , and blockage ratio β .

G. Effect of cylinder rotation on the flow field and hydrodynamic force

The rotation of the cylinder induced by the flow would affect the adjacent flow field in return. When cylinder rotates, a lubrication layer which is close to the cylinder surface will be produced because of the no-slip boundary condition.

1. Distribution of streamline

Figure 17 shows the streamline of the flow past a rotating cylinder and a static cylinder. A stagnant point appears at the position with azimuthal angle $\theta \approx \pi/2$ as shown in Fig. 17(a), which is different from the flow past a static cylinder as shown in Fig. 17(b). Comparing Figs. 17(a) and 17(b) with Figs. 17(e) and 17(f), as the Reynolds number increases, an obvious vortex appears behind the rotating cylinder, but no such vortex can be seen behind the static cylinder. As the Reynolds number continues to increase, a pair of large vortices appears behind the rotating cylinder as shown in

Fig. 17(g) and the same thing also happens in the case of static cylinder. The above facts indicate that the flow pattern is obviously different for the flow past a rotating cylinder and past a static cylinder when the Reynolds number is low, and such difference disappears with the increase of the Reynolds number.

At the same Reynolds number Re , the eccentricity ratio ε has an essential effect on the flow pattern for the flow past a rotating cylinder as shown in Figs. 17(a) and 17(c), i.e., the stagnant point disappears as the position of the cylinder is close to the centerline. However there is no obvious effect of eccentricity ratio on the flow pattern for the flow past a static cylinder as shown in Figs. 17(b) and 17(d).

2. Distribution of vorticity field

The vorticity fields of the flow past a rotating cylinder and a static cylinder at different Reynolds numbers are shown in Fig. 18. The distributions of vorticity undergo changes with the increase of the Reynolds number at a specific eccentricity ratio, and they are almost the same for the flow past a rotating cylinder and past a static cylinder.

3. Distribution of mean pressure distribution

The mean pressure distribution \bar{C}_p on the cylinder surface is shown in Fig. 19. When fluid flows past a cylinder at $\varepsilon = 4/8$, the difference in the mean pressure distribution

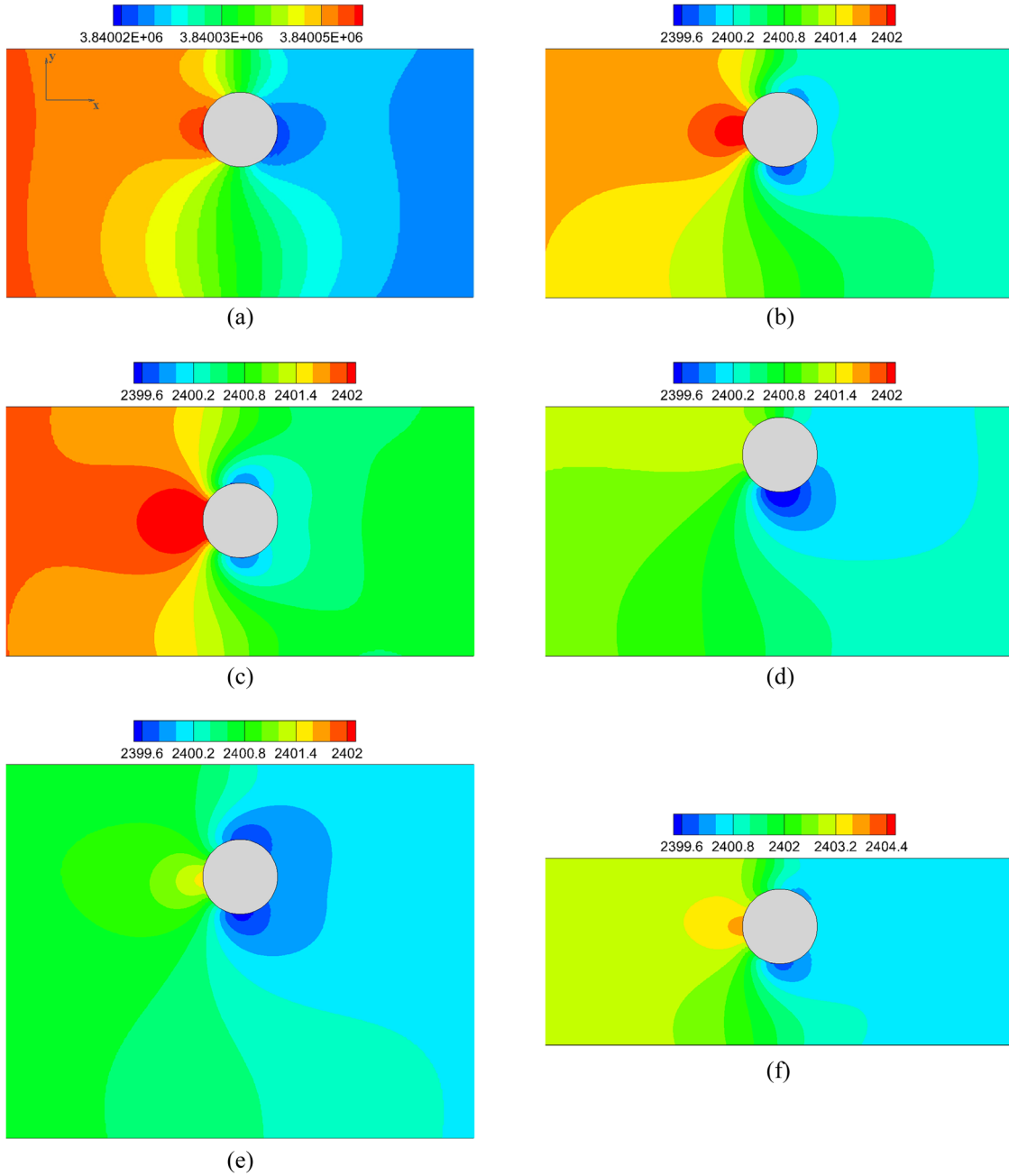


FIG. 16. Pressure contour near the cylinder. (a) $Re = 1$, $\varepsilon = 4/8$, $\beta = 0.3$; (b) $Re = 40$, $\varepsilon = 4/8$, $\beta = 0.3$; (c) $Re = 40$, $\varepsilon = 1/8$, $\beta = 0.3$; (d) $Re = 40$, $\varepsilon = 7/8$, $\beta = 0.3$; (e) $Re = 40$, $\varepsilon = 4/8$, $\beta = 0.2$; (f) $Re = 40$, $\varepsilon = 4/8$, $\beta = 0.4$.

between the rotating cylinder and static cylinder is nearly the same at $Re = 40$ as shown in Fig. 19(a), while the mean pressures on the upper and lower semi-cylinder become smaller and larger, respectively, at $Re = 200$ as shown in Fig. 19(c), leading to a smaller pressure difference between the two sides of the cylinder than that in the case of the static cylinder. When the cylinder is located in the vicinity of the wall ($\varepsilon = 7/8$) as shown in Figs. 19(b) and 19(d), a larger pressure difference between the two sides of the cylinder than that at $\varepsilon = 4/8$ appears at low and high Reynolds numbers, and the difference in the mean pressure distribution between the rotating cylinder and static cylinder is more obvious.

4. Drag coefficient

The rotation of the cylinder induced by the flow would affect the hydrodynamic force exerted on the cylinder. Tao and Bao²⁵ reported a significant drag reduction for the flow past two side-by-side arranged cylinders rotating about their axes. In the present study, we find that the variation of drag coefficient is more complicated. The comparison of drag coefficient C_D between rotating cylinder and static cylinder for different rotating Reynolds numbers Re and eccentricity ratios ε at $\beta = 0.3$ is listed in Table II, where $\Delta C_D = (C_{DR} - C_{DS})/C_{DS}$, and C_{DR} and C_{DS} are the drag coefficient for the rotating cylinder and static cylinder, respectively. It can be seen that, in general, the

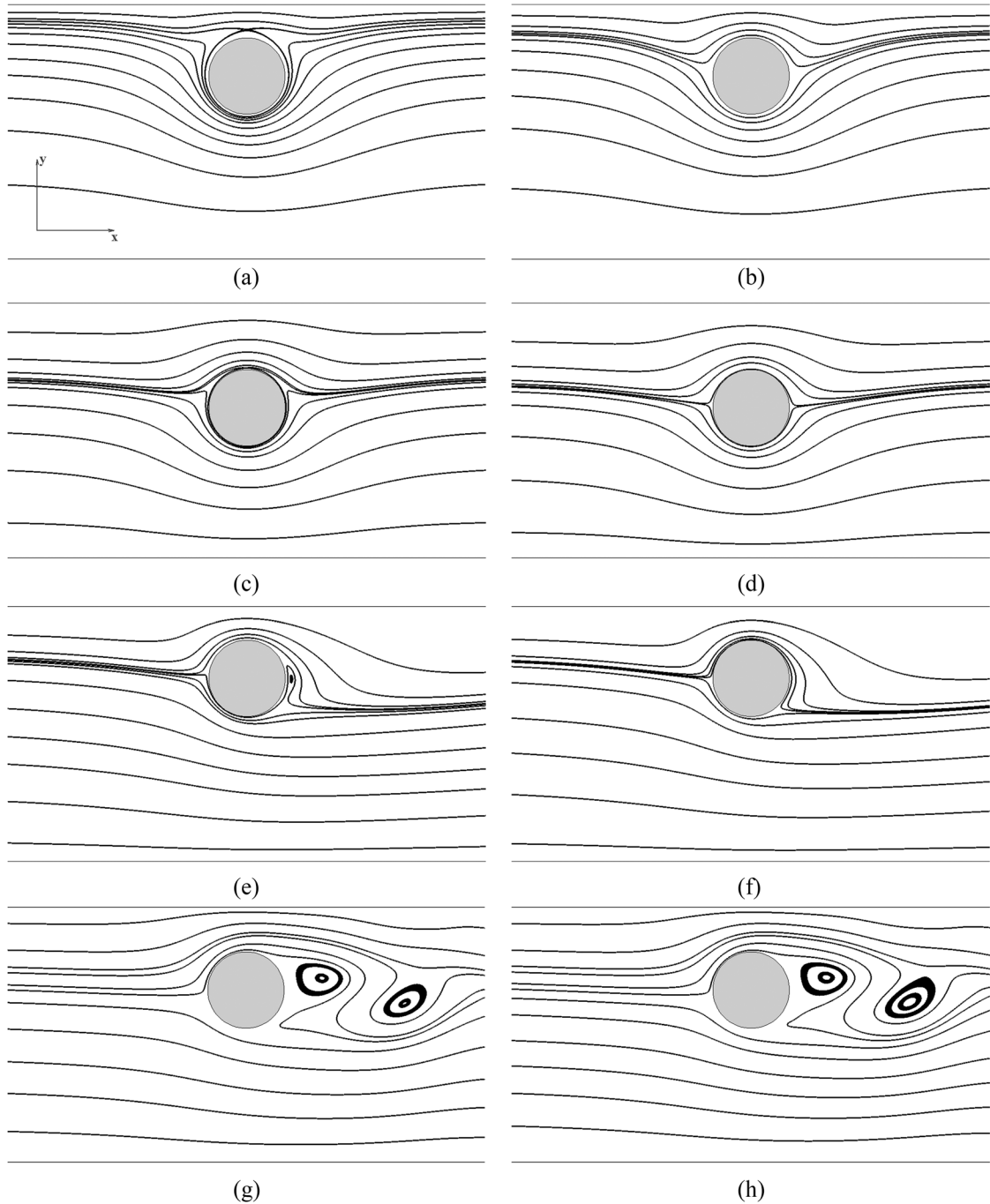


FIG. 17. Comparison of streamline of flow past a rotating cylinder and a static cylinder ($\beta = 0.3$). (a) Rotating cylinder ($Re = 1$, $\varepsilon = 5/8$); (b) static cylinder ($Re = 1$, $\varepsilon = 5/8$); (c) rotating cylinder ($Re = 1$, $\varepsilon = 2/8$); (d) static cylinder ($Re = 1$, $\varepsilon = 2/8$); (e) rotating cylinder ($Re = 40$, $\varepsilon = 5/8$); (f) static cylinder ($Re = 40$, $\varepsilon = 5/8$); (g) rotating cylinder ($Re = 200$, $\varepsilon = 5/8$); (h) static cylinder ($Re = 200$, $\varepsilon = 5/8$).

relative difference ΔC_D of drag coefficient between the rotating cylinder and static cylinder is small, and the maximum relative difference is 13%.

Figure 20 shows the relationship between ΔC_D and Reynolds number Re as well as eccentricity ratio ε . It can be seen that, at a low Reynolds number, the drag coefficient for the rotating cylinder is always smaller than that for the static cylinder at any eccentricity ratio, which is in accordance with the previous result.²⁵ However, when the Reynolds number is larger than 40, the drag coefficient for the rotating cylinder is larger than that for the static cylinder at a low eccentricity

ratio. As the eccentricity ratio increases and exceeds a critical value, the drag coefficient for the rotating cylinder begins to decrease and finally is smaller than that for the static cylinder. Such a critical value of the eccentricity ratio is dependent on the Reynolds number. Comparing with the relationship between the mean rotating velocity $\bar{\omega}$ and eccentricity ratio ε for different Reynolds numbers as shown in Fig. 6(a), we can find an interesting phenomenon that the change of the difference in drag coefficient C_D between the rotating cylinder and static cylinder is qualitatively similar to that of the mean rotating velocity $\bar{\omega}$. When the cylinder rotates clockwise and

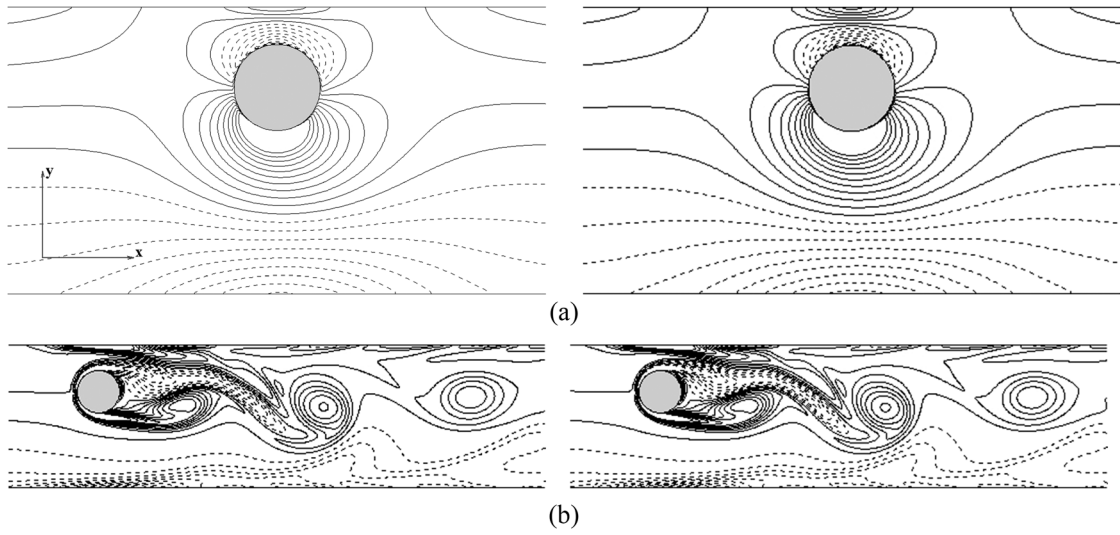


FIG. 18. Comparison of vorticity field of flow past a rotating cylinder and a static cylinder ($\beta = 0.3$). (a) $Re = 1$, $\epsilon = 5/8$ and (b) $Re = 200$, $\epsilon = 5/8$. [(a1) and (b1)] Rotating cylinder and [(a2) and (b2)] static cylinder.

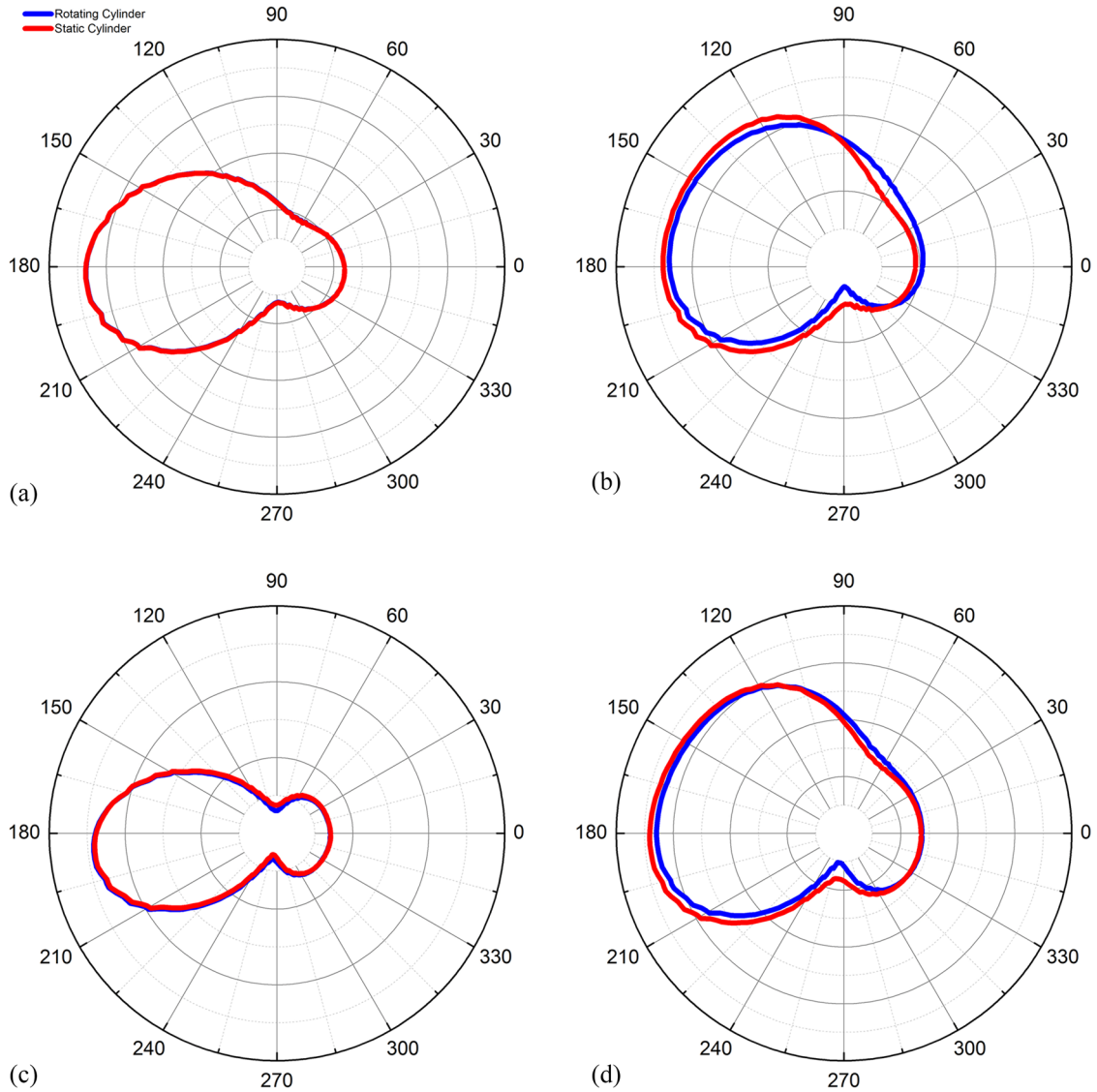


FIG. 19. Comparison of mean pressure coefficient distribution on the surface of cylinder ($\beta = 0.3$). (a) $Re = 40$, $\epsilon = 4/8$; (b) $Re = 40$, $\epsilon = 7/8$; (c) $Re = 200$, $\epsilon = 4/8$; (d) $Re = 200$, $\epsilon = 7/8$.

TABLE II. Comparison of drag coefficient between rotating cylinder and static cylinder at $\beta = 0.3$.

		$\varepsilon = 0/8$	$\varepsilon = 1/8$	$\varepsilon = 2/8$	$\varepsilon = 3/8$	$\varepsilon = 4/8$	$\varepsilon = 5/8$	$\varepsilon = 6/8$	$\varepsilon = 7/8$
Re = 0.1	Rotating cylinder	557.7	544.1	506.9	454.6	396.4	339.4	287.9	244.4
	Static cylinder	557.7	545.6	512	463.9	409.1	353.9	302.3	256.3
	ΔC_D (%)	0.00	-0.27	-1.00	-2.00	-3.10	-4.10	-4.76	-4.64
Re = 1	Rotating cylinder	55.84	54.5	50.81	45.6	39.79	34.1	28.94	24.57
	Static cylinder	55.84	54.64	51.32	46.55	41.08	35.57	30.4	25.78
	ΔC_D (%)	0.00	-0.26	-0.99	-2.04	-3.14	-4.13	-4.80	-4.69
Re = 10	Rotating cylinder	6.143	6.086	5.889	5.511	4.957	4.309	3.667	3.11
	Static cylinder	6.143	6.096	5.935	5.623	5.152	4.567	3.945	3.35
	ΔC_D (%)	0.00	-0.16	-0.78	-1.99	-3.78	-5.65	-7.05	-7.16
Re = 40	Rotating cylinder	2.368	2.358	2.329	2.285	2.211	2.029	1.694	1.36
	Static cylinder	2.368	2.358	2.328	2.282	2.215	2.083	1.842	1.547
	ΔC_D (%)	0.00	0.00	0.04	0.13	-0.18	-2.59	-8.03	-12.1
Re = 100	Rotating cylinder	1.579	1.571	1.542	1.502	1.452	1.396	1.284	0.967
	Static cylinder	1.579	1.571	1.54	1.495	1.441	1.383	1.305	1.112
	ΔC_D (%)	0.00	0.00	0.13	0.47	0.76	0.94	-1.61	-13.0
Re = 200	Rotating cylinder	1.370	1.358	1.319	1.265	1.199	1.113	1.049	0.86
	Static cylinder	1.371	1.358	1.317	1.258	1.185	1.098	1.035	0.942
	ΔC_D (%)	0.07	0.00	0.15	0.56	1.18	1.37	1.35	-8.70

counterclockwise, the drag coefficient for the rotating cylinder is larger and smaller than that for the static cylinder, respectively, which indicates that counterclockwise rotation of the cylinder has a drag reduction effect compared with the static cylinder.

5. Lift coefficient

Figure 21 shows the comparison of lift coefficient C_L between the rotating cylinder and static cylinder at $\beta = 0.3$. As shown in Fig. 21(a), the values of lift coefficient C_L are nearly the same for the rotating cylinder when $Re = 0.1$ and 1 and the situation is the same for the static cylinder. This indicates that the change of the Reynolds number has

no effect on the lift coefficient at very low Reynolds number. At $Re < 10$, the absolute value of lift coefficient for the rotating cylinder is larger than that for the static cylinder, and both lift coefficients are always negative. All absolute values of lift coefficient increase and then decrease with an increase in the eccentricity ratio, indicating that there exists a position between the centerline and the wall (i.e., $\varepsilon = 4/8$), at which the lift force exerted on the cylinder by the fluid is the largest. As shown in Fig. 21(b), the values of lift coefficient are nearly the same for the rotating cylinder and the static cylinder for $\varepsilon < 4/8$ and $Re = 40$ and the absolute value of lift coefficient for the rotating cylinder is larger than that for the static cylinder for $\varepsilon > 4/8$. For $Re = 100$ and 200, the absolute values of lift coefficients for the rotating cylinder are always larger than that for the static cylinder. Comparing with Fig. 21(a), we can see that the relative difference of lift coefficient between the rotating cylinder and static cylinder is highly related to the mean rotating velocity $\bar{\omega}$.

6. Relationship between drag coefficient and lift coefficient

When the cylinder rotates counterclockwise and clockwise, the lift coefficients are reduced and increased compared with the static cylinder, which is mainly attributed to the Magnus effect generated by the rotation of the cylinder. Figure 22 shows the phase space of drag coefficient C_D and lift coefficient C_L at $Re = 200$ and $\beta = 0.3$. As the eccentricity ratio increases, the dumbbell shape of $C_D - C_L$ phase space becomes untwisted because the alternate vortex shedding is suppressed and only a single row of vortex sheds behind the cylinder as the position, at which the cylinder is located, moves toward the wall.

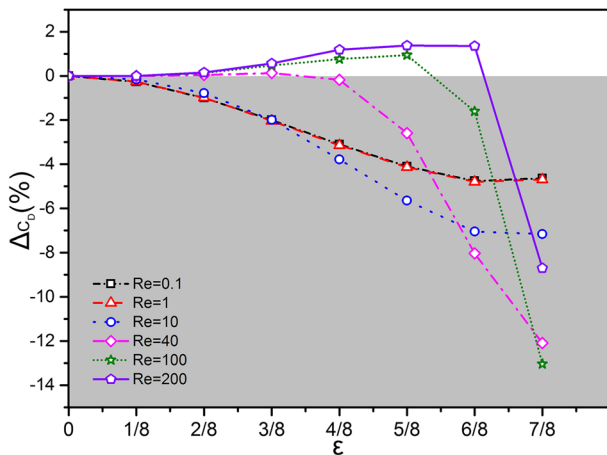


FIG. 20. Relative difference of drag coefficient between rotating cylinder and static cylinder ($\beta = 0.3$).

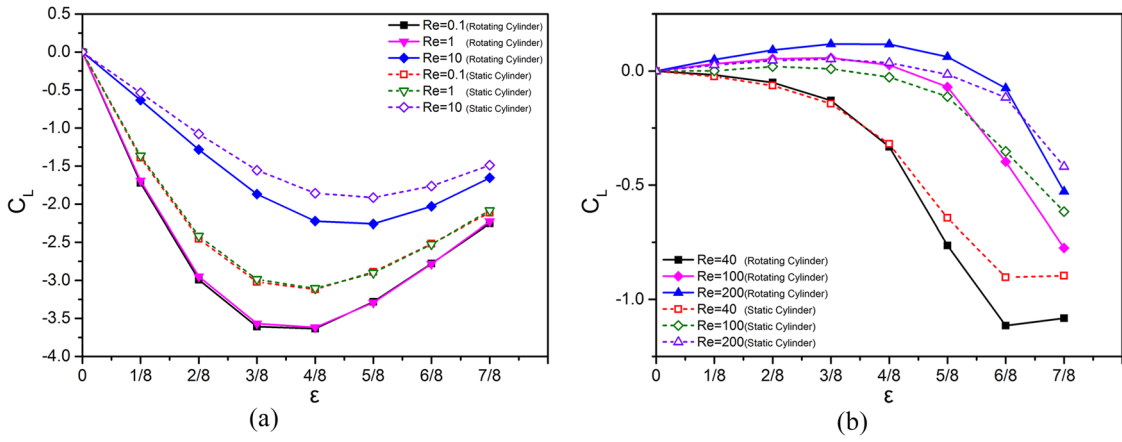


FIG. 21. Comparison of lift coefficient C_L between the rotating cylinder and static cylinder ($\beta = 0.3$). (a) $0.1 \leq Re \leq 10$ and (b) $40 \leq Re \leq 200$.

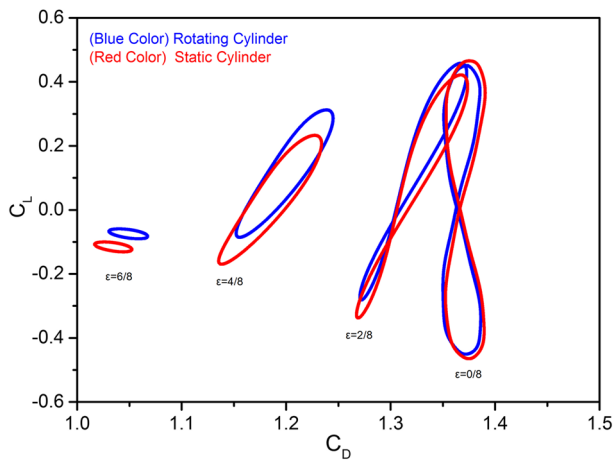


FIG. 22. Phase space of drag coefficient C_D and lift coefficient C_L at $Re = 200$ and $\beta = 0.3$.

V. CONCLUSIONS

Flow past a center-pinned freely rotatable cylinder asymmetrically confined in a two dimensional channel is simulated with the lattice Boltzmann method. The effect of Reynolds number Re , eccentricity ratio ϵ , and blockage ratio β on the rotating velocity $\bar{\omega}$ is discussed, and the mechanism of rotational behavior is also analyzed. The following conclusions can be drawn.

Fluid inertia plays a critical role in making the cylinder rotate in an abnormal way. At a low Reynolds number, the cylinder rotates counterclockwise and the changes of mean rotating velocity with eccentricity ratio are nearly the same. When the Reynolds number increases and exceeds a certain value, the mean rotating velocities decrease quickly and finally change from normally counterclockwise to abnormally clockwise. At $Re < 10$, the mean rotating velocity increases with an increase in the eccentricity ratio, except the case in the vicinity of the wall. At $Re > 40$, in the region between the separatrix and the centerline, the cylinder rotates faster in a clockwise direction and then slows down after reaching a maximum with an increase in the eccentricity ratio. In the region between the separatrix and the wall, the cylinder rotates counterclockwise and the rotating velocity becomes larger with increasing the eccentricity ratio. With an increase in the Reynolds number,

the maximum clockwise rotating velocity becomes larger and the position where the rotating velocity reaches its maximum shifts toward the wall. The counterclockwise rotating velocity increases with an increase in the blockage ratio. The maximum clockwise rotating velocity does not occur in the case with the minimum blockage ratio but in the case with an intermediate blockage ratio of 0.3. Generally, the critical Reynolds number is low when the cylinder is located near the channel centerline and increases accordingly with an increase in the eccentricity ratio. The separatrix generally moves upward when the blockage effect becomes more severe.

The competition between the positive shear stress and negative shear stress determines the rotating behavior of the cylinder. In the vicinity of the wall, the positive shear stress is much larger than the negative shear stress, which makes the cylinder rotate counterclockwise. In the region near the centerline, the positive shear stress does not play a dominant role though it is still slightly larger than the negative shear stress. The surface area subjected to the negative shear stress is larger than that subjected to the positive shear stress at a high Reynolds number, so the torque exerted on the cylinder produced by the negative shear stress would exceed that by the positive shear stress. The competition between the above two factors makes the occurrence of anomalous rotation of the cylinder at a high Reynolds number. The shear stress increases with increasing the blockage ratio at a high Reynolds number, which makes the cylinder rotate counterclockwise faster. The maximum positive shear stress decreases slightly with an increase in the eccentricity ratio for different Reynolds numbers, but it reduces significantly with an increase in the Reynolds number for different eccentricity ratios, which contributes to the fact that the counterclockwise or clockwise rotating velocity reaches its maximum at an intermediate eccentricity ratio. As the Reynolds number increases, the single minimum pressure zone behind the cylinder breaks into two pieces, and the moving of the minimum pressure zone on the upper semi-cylinder lags slightly behind the one on the lower semi-cylinder. It creates a difference in the surface areas subjected to the negative and positive shear stress. As the Reynolds number increases further, the two minimum pressure zones are more symmetrical and their values are close to the same level. Therefore, the difference in the values between the positive and negative

shear stress decreases as the Reynolds number increases. As the eccentricity ratio increases, the minimum pressure zone on the upper semi-cylinder becomes smaller and finally disappears, while that on the lower semi-cylinder becomes larger. The pressure drop along the lower semi-cylinder is much larger than that along the upper semi-cylinder at a higher eccentricity ratio, which makes the positive shear stress play a dominant role in this region. Meanwhile, the maximum pressure zone shifts counterclockwise and the minimum pressure zone on the upper semi-cylinder shifts leeward, leading to a variation of cylinder surface areas subjected to the positive and negative shear stress. So the rotational behavior of the cylinder is dependent on the distribution of shear stress exerted on the cylinder, while the shear stress is affected by the pressure difference on the cylinder surface, the shift of maximum and minimum pressure zones, and the shift of stagnant points and separate points.

The flow pattern is obviously different for the flow past a rotating cylinder and past a static cylinder when the Reynolds number is low, and such difference disappears with an increase in the Reynolds number. At a low Reynolds number, a stagnant point appears at the position with azimuthal angle $\theta \approx \pi/2$. As the Reynolds number increases, an obvious vortex appears behind the rotating cylinder. As the Reynolds number continues to increase, a pair of large vortices appears behind the rotating cylinder, which is similar to the case of the static cylinder. When the cylinder rotates clockwise and counterclockwise, the drag coefficient for the rotating cylinder is larger and smaller than that for the static cylinder, respectively. Only the counterclockwise rotation of the cylinder has a drag reduction effect compared with that of the static cylinder. Similarly, the difference in lift coefficient between the rotating cylinder and static cylinder is highly related to the mean rotating velocity.

ACKNOWLEDGMENTS

This work was supported by the Major Program of the National Natural Science Foundation of China with Grant Nos. 11632016 and 91634103.

- ¹T. Sarpkaya, "A critical review of the intrinsic nature of vortex-induced vibrations," *J. Fluids Struct.* **19**, 389–447 (2004).
- ²C. H. K. Williamson and R. Govardhan, "Vortex-induced vibrations," *Annu. Rev. Fluid Mech.* **36**, 413–455 (2004).
- ³H. J. Lugt, "Autorotation," *Annu. Rev. Fluid Mech.* **15**, 123–147 (1983).
- ⁴M. Sen, D. Wajerski, and M. A. Gad-el-Hak, "A novel pump for MEMS applications," *J. Fluids Eng.* **118**, 624–627 (1996).
- ⁵B. Zhang, X. M. Liu, and J. J. Sun, "Topology optimization design of non-Newtonian roller-viscous micropumps type," *Struct. Multidiscip. Optim.* **53**, 409–424 (2016).
- ⁶P. Bagchi and S. Balachandar, "Effect of free rotation on the motion of a solid sphere in linear shear flow at moderate Re," *Phys. Fluids* **14**, 2719–2737 (2002).
- ⁷D. R. Oliver, "Influence of particle rotation on radial migration in the Poiseuille flow of suspensions," *Nature* **194**, 1269–1271 (1962).
- ⁸H. J. Lugt, "Autorotation of an elliptic cylinder about an axis perpendicular to the flow," *J. Fluid Mech.* **99**, 817–840 (1980).
- ⁹B. W. Skews, "Autorotation of many-sided bodies in an airstream," *Nature* **352**, 512–513 (1991).
- ¹⁰R. Mittal, V. Seshadri, and H. S. Udaykumar, "Flutter, tumble and vortex induced autorotation," *Theor. Comput. Fluid Dyn.* **17**, 165–170 (2004).
- ¹¹T. G. Zaki, M. Sen, and M. A. Gad-el-Hak, "Numerical and experimental investigation of flow past a freely rotatable square cylinder," *J. Fluids Struct.* **8**, 555–582 (1994).
- ¹²S. Ryu and G. Iaccarino, "Vortex-induced rotations of a rigid square cylinder at low Reynolds numbers," *J. Fluid Mech.* **813**, 482–507 (2017).
- ¹³S. Z. Wang, L. D. Zhu, X. Zhang, and G. W. He, "Flow past two freely rotatable triangular cylinders in tandem arrangement," *J. Fluids Eng.* **133**, 081202 (2011).
- ¹⁴S. Mittal, "Control of flow past bluff bodies using rotating control cylinders," *J. Fluids Struct.* **15**, 291–326 (2001).
- ¹⁵J. C. Schulmeister, J. M. Dahl, G. D. Weymouth, and M. S. Triantafyllou, "Flow control with rotating cylinders," *J. Fluid Mech.* **825**, 743–763 (2017).
- ¹⁶H. Juarez, R. Scott, R. Metcalfe, and B. Bagheri, "Direct simulation of freely rotating cylinders in viscous flows by high-order finite element methods," *Comput. Fluids* **29**, 547–582 (2000).
- ¹⁷A. Einstein, "Eine neue Bestimmung der Moleküldimensionen," *Ann. Phys.* **324**, 289 (1906).
- ¹⁸A. Einstein, "Berichtigung zu meiner Arbeit: 'Eine neue Bestimmung der Moleküldimensionen,'" *Ann. Phys.* **339**, 591 (1911).
- ¹⁹A. J. Goldman, R. G. Cox, and H. Brenner, "Slow viscous motion of a sphere parallel to a plane wall. I. Motion through quiescent fluid," *Chem. Eng. Sci.* **22**, 637–651 (1967).
- ²⁰Y. J. Liu, J. Nelson, J. Feng, and D. D. Joseph, "Anomalous rolling of spheres down an inclined plane," *J. Non-Newtonian Fluid Mech.* **50**, 305–329 (1993).
- ²¹P. Singh and D. D. Joseph, "Sedimentation of a sphere near a vertical wall in an Oldroyd-B fluid," *J. Non-Newtonian Fluid Mech.* **94**, 179–203 (2000).
- ²²H. H. Hu, "Motion of a circular cylinder in a viscous liquid between parallel plates," *Theor. Comput. Fluid Dyn.* **7**, 441–455 (1995).
- ²³J. R. T. Seddon and T. Mullin, "Reverse rotation of a cylinder near a wall," *Phys. Fluids* **18**, 041703 (2006).
- ²⁴C. Sun, T. Mullin, L. Van Wijngaarden, and D. Lohse, "Drag and lift forces on a counter-rotating cylinder in rotating flow," *J. Fluid Mech.* **664**, 150–173 (2010).
- ²⁵J. Tao and Y. Bao, "Drag reduction of wake flow by shear-driven rotation," *Phys. Rev. E* **87**(2), 023013 (2013).
- ²⁶S. Y. Chen and G. D. Doolen, "Lattice Boltzmann method for fluid flow," *Annu. Rev. Fluid Mech.* **30**, 329–364 (1998).
- ²⁷C. K. Aidun and J. R. Clausen, "Lattice-Boltzmann method for complex flows," *Annu. Rev. Fluid Mech.* **42**(1), 439–472 (2010).
- ²⁸Y. H. Qian, D. D'Humieres, and P. Lallemand, "Lattice BGK models for Navier-Stokes equation," *Europhys. Lett.* **17**(6), 479–484 (1992).
- ²⁹D. Z. Yu, R. W. Mei, and W. Shyy, "A unified boundary treatment in Lattice Boltzmann method," AIAA Paper 2003-0953, 2003.
- ³⁰M. Cheng and L. S. Luo, "Characteristics of two-dimensional flow around a rotating circular cylinder near a plane wall," *Phys. Fluids* **19**, 063601 (2007).
- ³¹B. H. Wen, C. Y. Zhang, Y. S. Tu, C. L. Wang, and H. P. Fang, "Galilean invariant fluid–solid interfacial dynamics in lattice Boltzmann simulations," *J. Comput. Phys.* **266**, 161–170 (2014).
- ³²S. Tao, J. J. Hu, and Z. L. Guo, "An investigation on momentum exchange methods and refilling algorithms for lattice Boltzmann simulation of particulate flows," *Comput. Fluids* **133**, 1–14 (2016).
- ³³C. Peng, Y. H. Teng, B. Hwang, Z. L. Guo, and L. P. Wang, "Implementation issues and benchmarking of lattice Boltzmann method for moving rigid particle simulations in a viscous flow," *Comput. Math. Appl.* **72**(2), 349–374 (2016).
- ³⁴M. Sahin and R. G. Owens, "A numerical investigation of wall effects up to high blockage ratios on two-dimensional flow past a confined circular cylinder," *Phys. Fluids* **16**(5), 1305–1320 (2004).
- ³⁵D. Stojkovic, M. Breuer, and F. Durst, "Effect of high rotation rates on the laminar flow around a circular cylinder," *Phys. Fluids* **14**, 3160–3178 (2002).
- ³⁶H. M. Badr, S. C. R. Dennis, and P. J. S. Young, "Steady and unsteady flow past a rotating circular cylinder at low Reynolds numbers," *Comput. Fluids* **17**, 579–609 (1989).
- ³⁷S. K. Panda and R. P. Chhabra, "Laminar flow of power-law fluids past a rotating cylinder," *J. Non-Newtonian Fluid Mech.* **165**(21–22), 1442–1461 (2010).
- ³⁸S. B. Paramane and A. Sharma, "Numerical investigation of heat and fluid flow across a rotating circular cylinder maintained at constant temperature in 2-D laminar flow regime," *Int. J. Heat Mass Transfer* **52**, 3205–3216 (2009).
- ³⁹S. Kang, H. Choi, and S. Lee, "Laminar flow past a rotating circular cylinder," *Phys. Fluids* **11**, 3312–3321 (1999).
- ⁴⁰K. Shaafaa, S. N. Naik, and N. Vengadesan, "Effect of rotating cylinder on the wake-wall interactions," *Ocean Eng.* **139**, 275–286 (2017).
- ⁴¹P. C. Bollada and T. N. Phillips, "A physical decomposition of the stress tensor for complex flows," *Rheol. Acta* **47**(7), 719–725 (2008).